IET Radar, Sonar & Navigation

WILEY

The Institution of Engineering and Technology

ORIGINAL RESEARCH OPEN ACCESS

Statistical Analysis of Performance of Optimisation-Based SAR Autofocus

Patrick Haughey | Mikhail Gilman | Semyon Tsynkov

Department of Mathematics, North Carolina State University, Raleigh, North Carolina, USA

Correspondence: Patrick Haughey (pmhaughe@ncsu.edu)

Received: 20 February 2025 | **Revised:** 4 April 2025 | **Accepted:** 14 April 2025

Handling Editor: Hugh Griffiths

Funding: This work was supported by the US Air Force Office of Scientific Research (AFOSR) under awards nos. FA9550-23-1-0101 and FA9550-24-1-0172. The work of the first author is also supported by NASA under award no. 80NSSC20M0095 (CFDA 43.008) through the North Carolina Space Grant, National Space Grant College and Fellowship Programme Opportunities in NASA STEM (FY 2020–2024).

Keywords: environmental factors | inverse synthetic aperture radar (ISAR) | ionospheric disturbances | optimisation | phase estimation | statistical analysis

ABSTRACT

Transionospheric SAR autofocus is a variational algorithm designed to circumvent the deficiencies of conventional autofocus techniques in correcting the distortions of spaceborne SAR images due to ionospheric turbulence. It has demonstrated superior performance in a variety of computer-simulated imaging scenarios. In the current work, we conduct a systematic statistical analysis of transionospheric SAR autofocus aimed at corroborating its robustness and identifying limitations and sensitivities across a broad range of factors that affect the autofocus performance. We employ the range-compressed domain representation where the target reflectivity, antenna signal, and the phase screen depend only on the azimuthal coordinate. The three main factors included in the study are the levels of turbulent perturbations, clutter, and noise. We use the normalised cross correlation (NCC), integrated sidelobe ratio (ISLR), and peak desynchronisation (PD) as a-posteriori performance metrics. A key objective of the current analysis, beyond assessing the autofocus performance, is to identify the directions of how to further improve the algorithm, in terms of both the quality of focusing and associated computational cost.

1 | Introduction

Autofocus is a procedure whereby an imaging system produces crisp images without user intervention. In optical systems, focusing is achieved by adjusting the lens. An autofocus that adjusts the lens would typically rely on multiple acquisitions with subsequent registration of split images and deriving the required adjustment based on the registration data. Imaging radars, such as synthetic aperture radar (SAR), provide a viable supplement to optical systems when the latter suffer from their inherent limitations. In particular, radars can obtain images with no external illumination, as well as through the clouds or dust. In SAR imaging, autofocus is realised via adjustment of the signal processing procedure.

The frequencies used by satellite-based synthetic aperture radars are in the microwave range, typically from P-band, 0.225–0.39 GHz, to X-band, 6.2–10.9 GHz, in the pre-1978 NATO nomenclature (or, alternatively, between B-band and I-band in the current nomenclature). In fact, there are higher frequency radars that operate in the Ka-band (K-band in the present NATO nomenclature) and even W-band (M-band in the present NATO nomenclature), such as the PAMIR-Ka and MIRANDA-94 systems [1]. However, these higher frequency bands are used primarily for airborne platforms because of the increased atmospheric attenuation of radar signals for carrier frequencies above the X-band (see, e.g., [[2], Chapter 12]). Frequencies below the P-band are problematic because of the difficulties of deploying an antenna of the required size in space.

The ionosphere is a layer of dilute cold plasma that starts at approximately 90 *km* above the Earth surface and extends several hundred kilometres further upwards. The propagation of radar signals in the ionosphere becomes dispersive, which, in turn, causes distortions of the resulting spaceborne SAR images. The distortions can be categorised into those due to the background ionosphere and those due to the ionospheric turbulence. While very different from optical distortions on the substance, the former can still be mitigated efficiently via multiple acquisitions (e.g., dual-carrier probing) and registration, see refs. [3, 4] and ([5], Chapter 3). The latter are a lot more difficult to handle. The main reason is that SAR signals propagating between the antenna and different locations on the target travel through different regions of turbulent plasma and thus acquire different perturbations. In this case, the corrections obtained with the help of dual-carrier probing appear insufficient.

A variety of SAR autofocus algorithms have been developed and successfully deployed for correcting the distortions of SAR images due to uncertainties of antenna trajectory [6–8]. These algorithms typically operate under the assumption that phase errors are spatially invariant across the entire SAR image. As a result, they can estimate a correction phase for a particular antenna position by averaging the responses from all strong scatterers, thereby mitigating the effects of noise and clutter. However, those algorithms prove inefficient for distortions due to the ionospheric turbulence because the aforementioned assumption breaks down [9, 10]. Indeed, in the case of propagation through ionospheric turbulence, there will be different distortions that correspond to one and the same antenna position but different signal travel paths connecting it to different target locations within the beam footprint.

The effect of ionospheric turbulence on radar signals is often referred to in the literature as scintillation phase errors (SPE). Mitigation of image distortions due to the dispersive propagation of radar signals requires reconstruction and compensation of the actual perturbations. If polarimetric data are available, the perturbation function can be estimated by measuring the Faraday rotation (FR), see, for example, [10]. In the absence of FR or any other data about the instantaneous distribution of the electron number density in the ionosphere, the reconstruction has to be performed based on the received radar signals. The insufficient capacity of conventional autofocus algorithms (such as phase gradient autofocus (PGA) [6]) to mitigate the distortions of spaceborne SAR images due to SPE is a well-known hard problem, see, for example, the recent survey paper [11].

In our work [9], we proposed a first viable solution to this problem—a variational autofocus algorithm that specifically takes into account the nature of turbulence-induced signal distortions, that is, their dependence on both the antenna coordinates and target coordinates. In the core of the algorithm of ref. [9], there is an optimisation problem whose solution yields the correction for SPE. Yet the algorithm of ref. [9] is not a data-fitting methodology (such as full waveform inversion) as it explicitly relies on a nonvariational SAR imaging functional for reconstructing the unknown ground reflectivity. Compared to the standard SAR imaging functionals (see, e.g., [12] or [5], Chapter 2), the one we employ in ref. [9] contains an SPE correction in a parametric form, with the parameters being subsequently varied to achieve the best image focusing in the course of optimisation.

The algorithm of ref. [9] uses a number of simplifying assumptions, first and foremost, a 'condensed' representation of the ionosphere by means of a phase screen. A justification for using the phase screens for the analysis of transionospheric SAR imaging is provided in our work [13], while in an earlier paper [14] we proposed a method for choosing the phase screen elevation. It relies on a certain type of interferometric SAR processing and positions the screen where the ionosphere is most turbulent. The second simplification is the use of a single range bin for the range-compressed domain model where the target reflectivity, antenna signal, and phase screen density are represented by univariate functions. This simplification is justified by our previous finding that the ionospheric turbulence affects the SAR imaging in azimuth much stronger than that in range (see [5], Chapter 4 and [15]). Yet the analysis of (ref. [5], Chapter 4) and ref. [15] did not account for ionospheric anisotropies due to the magnetic field of the Earth. Consequently, the use of the range compressed formulation in the case where the SPE is anisotropic [16] could require further justification and may eventually prove insufficient. One possible PGA-based approach for compensation of distortions due to anisotropic and spatially varying two-dimensional SPE has been examined for ALOS-2 PALSAR-2 imagery in ref. [17].

The optimisation-based autofocus of ref. [9] has demonstrated a robust performance for various computer-simulated SAR imaging scenarios. Moreover, in the recent work [18], we have compared it against a more advanced implementation of the conventional autofocus that involves a two-step processing based on screen projection [19]. The optimisation-based method of ref. [9] offered a consistent advantage over [19] in the quality of focusing.

While the performance of the optimisation-based method of ref. [9] has been shown superior, the number of cases investigated as of yet is still rather limited. Therefore, the purpose of the current study is to conduct a statistical analysis of the algorithm of ref. [9] and corroborate its robustness, as well as identify limitations and sensitivities, across a broad range of factors that affect its performance. The rationale for using a statistical framework is that the ionospheric turbulence is modelled stochastically and so are the clutter and noise, which are the other two important factors that can affect the quality of focusing. In addition to assessing the autofocus performance, we expect that the results of the study will provide guidance on how to further improve it, in terms of both image quality and computational cost.

The rest of the paper is structured as follows. We begin by establishing the mathematics of SAR imaging, followed by the theoretical development of an ionospheric phase screen model. Next, we outline the setup for numerical experiments, detailing the data generation process with varying levels of ionospheric turbulence, clutter, and noise. Then we choose the cost function for optimisation and discuss the rationale behind our choice. We also discuss the selection and relevance of image quality metrics for evaluating the effectiveness of the autofocus algorithm, as well as the use of mutual information to assess the dependencies between specific perturbation factors and residual distortions. In the second part of the paper, we exhibit the results. We demonstrate the ability of our autofocus algorithm to generate a high quality approximation of the true ground reflectivity under various levels of turbulence, clutter, and noise. Namely, by minimising the cost function we can substantially improve the quality of image focusing under increasing and compounding levels of perturbations. Toward the end, we summarise our findings and discuss how the results of the statistical study and mutual information insights can inform future improvements to the autofocus algorithm, in particular, via redefining the optimisation procedure.

2 | Governing Equations

The radar antenna (mounted on a satellite) transmits frequency-modulated pulses of microwave radiation

$$P(t) = A(t)\exp(-\mathrm{i}\omega_0 t), \tag{1}$$

where $A(t)$ is narrow-band as compared to the (angular) frequency of the carrier: $|\mathrm{d}A/\mathrm{d}t| \ll \omega_0|A|$. After dispersive propagation from the radar antenna at $\boldsymbol{X}$ to a single point scatterer at $\boldsymbol{Z}_0$ and back, the return signal in the geometrical optics (GO) approximation is expressed as follows:

$$U^{\mathrm{sc}}(t,\boldsymbol{X}) = \nu_0\tilde{A}(t - t_{\mathrm{gr}})\exp\left[-\mathrm{i}\omega_0\left(t - t_{\mathrm{ph}}\right)\right], \tag{2}$$

where ν_0 is the scatterer reflectivity that also includes geometric attenuation, $\tilde{A}(t)$ is somewhat different from $A(t)$ due to the dispersion of waves within the signal bandwidth (see ref. [5], Chapter 3), and the phase and group two-way signal travel times are given by the following:

$$t_{\mathrm{ph,gr}} \equiv t_{\mathrm{ph,gr}}(\boldsymbol{X},\boldsymbol{Z}_0) = 2\int_{\boldsymbol{X}}^{\boldsymbol{Z}_0}\frac{\mathrm{d}l}{v_{\mathrm{ph,gr}}(\boldsymbol{r})}. \tag{3}$$

In Equation (3), $\boldsymbol{r}$ traces the ray path between $\boldsymbol{X}$ and $\boldsymbol{Z}_0$, v_{ph} and v_{gr} are the local phase and group velocities of electromagnetic pulses, and $\mathrm{d}l$ is the length differential along the ray. For the Earth's ionosphere, the phase and group velocities are close to the speed of light c:

$$\begin{gathered}\frac{v_{\mathrm{gr}}(\boldsymbol{r})}{c} \approx 1 - Kn_{\mathrm{e}}(\boldsymbol{r}), \quad \frac{v_{\mathrm{ph}}(\boldsymbol{r})}{c} \approx 1 + Kn_{\mathrm{e}}(\boldsymbol{r}),\\ \text{where}\quad Kn_{\mathrm{e}}(\boldsymbol{r}) \equiv \frac{1}{2}\frac{4\pi e^2}{m_{\mathrm{e}}\omega_0^2}\cdot n_{\mathrm{e}}(\boldsymbol{r}) \ll 1.\end{gathered} \tag{4}$$

In formulae (4), $-e$ and m_{e} are the electron charge and mass, respectively, and $n_{\mathrm{e}}(\boldsymbol{r})$ is the electron number density. We see that the factor K in Equation (4) rapidly decreases as the carrier frequency increases: $K \propto \omega_0^{-2}$ (see, e.g. [5, 20]). This helps explain why the lower frequency spaceborne SAR systems, such as P-band and L-band, are more susceptible to ionospheric distortions and, in particular, more likely to require autofocus for correcting the turbulence-induced errors than higher frequency systems such as X-band.

For a distributed scatterer with reflectivity $\nu(\boldsymbol{Z})$, Formula (2) is modified as follows:

$$\begin{aligned}U^{\mathrm{sc}}(t,\boldsymbol{X}) = \iint_{\text{2D beam footprint}} &\nu(\boldsymbol{Z})\tilde{A}\left[t - t_{\mathrm{gr}}(\boldsymbol{X},\boldsymbol{Z})\right]\\ &\times\exp\left[-\mathrm{i}\omega_0\left(t - t_{\mathrm{ph}}(\boldsymbol{X},\boldsymbol{Z})\right)\right]\,\mathrm{d}^2\boldsymbol{Z}.\end{aligned} \tag{5}$$

SAR image [to be defined in Equation (14)] is an approximate reconstruction of the unknown reflectivity $\nu(\boldsymbol{Z})$, where $U^{\mathrm{sc}}(t,\boldsymbol{X}_i)$ recorded for a certain set of locations $\{\boldsymbol{X}_i\}$ is used as data. For the analysis in this work, the data is generated numerically via Equation (2). We assume that the set $\{\boldsymbol{X}_i\}$, called the synthetic aperture, is spread over a segment of the antenna trajectory (satellite orbit) with the length L_{SA}. While L_{SA} is a parameter of the signal processing procedure, it is physically reasonable to set it approximately equal to the size of the beam footprint, such that the inversion uses the data affected by the unknown reflectivity.

The standard approach to transionospheric SAR inversion requires precise knowledge of $t_{\mathrm{ph}}(\boldsymbol{X}_i,\boldsymbol{Z})$ and $t_{\mathrm{gr}}(\boldsymbol{X}_i,\boldsymbol{Z})$. However, if $n_{\mathrm{e}}(\boldsymbol{r})$ is unknown, formulae (3) cannot be used directly, and the problem becomes significantly more complicated (see ref. [5], Chapter 3). In this work, we make several significant simplifications of the problem statement.

The first simplification aims at $t_{\mathrm{ph}}(\boldsymbol{X},\boldsymbol{Z})$ given by Formula (3) and involves the concept of a phase screen. The latter replaces the electron number density function $n_{\mathrm{e}}(\boldsymbol{r})$ in Equation (4) with a two-dimensional representation, as if the Earth's ionosphere were collapsed vertically into an infinitesimally thin sheet. Figure 1 illustrates the full-fledged three-dimensional geometry of spaceborne SAR imaging with a phase screen.

The second major simplification involves formulating the SAR imaging in the range compressed domain (see ref. [14], Appendix A for detail). Essentially, this means that we restrict the target to a single narrow range bin parallel to the satellite orbit where the reflectivity depends on the coordinate along this bin, called the azimuthal coordinate, see Figure 1. The range bin is identified by the distance R (also called the distance of closest approach) between it and the orbit. It can be shown [14] that the dependence of $U^{\mathrm{sc}}(t,\boldsymbol{X})$ on t can be eliminated by convolving with a delayed and complex conjugated replica of the transmitted signal $\overline{P(t-2R/c)}$, such that the double integration over the target in Equation (5) is reduced to the integration over the range bin:

$$u(X) = \int_{\text{1D beam footprint}} \nu(Z)\exp\left[\mathrm{i}\omega_0\left(t_{\mathrm{ph}}(\boldsymbol{X},\boldsymbol{Z}) - 2R/c\right)\right]\mathrm{d}Z, \tag{6}$$

where X and Z are the scalar azimuthal coordinates of the antenna and the target, respectively. As indicated in Section 1, a key rationale for considering the range compressed formulation is that the ionospheric turbulence has been shown to affect the SAR imaging in azimuth a lot stronger than in range (see ref. [5], Chapter 4 and [15]).

In Figure 1, we are showing the slant plane related to the selected range bin. This plane is defined as containing the orbit (approximated by a straight line) and the target (a point within the bin). The phase screen intersects the slant plane at a straight line on a certain elevation ξ relative to the orbit elevation, such

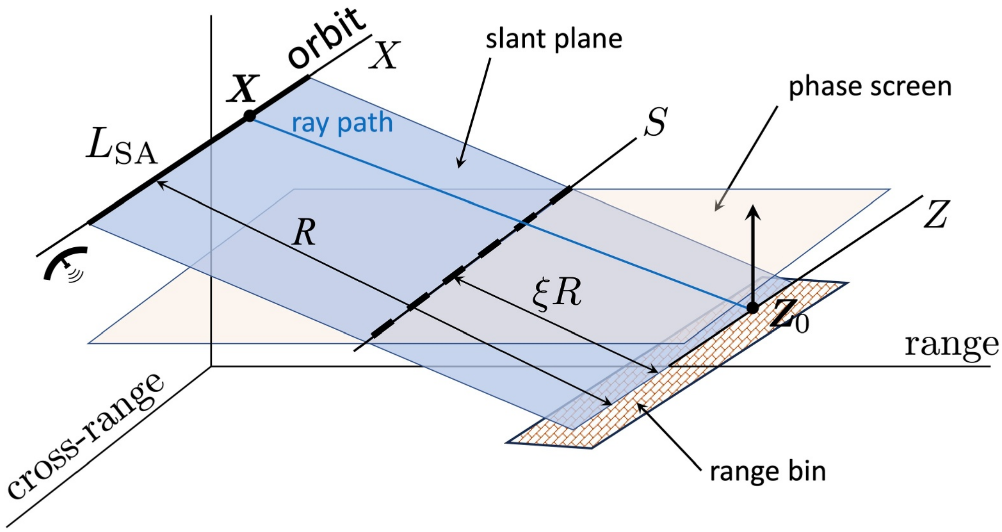

FIGURE 1 | Three-dimensional SAR geometry with a phase screen.

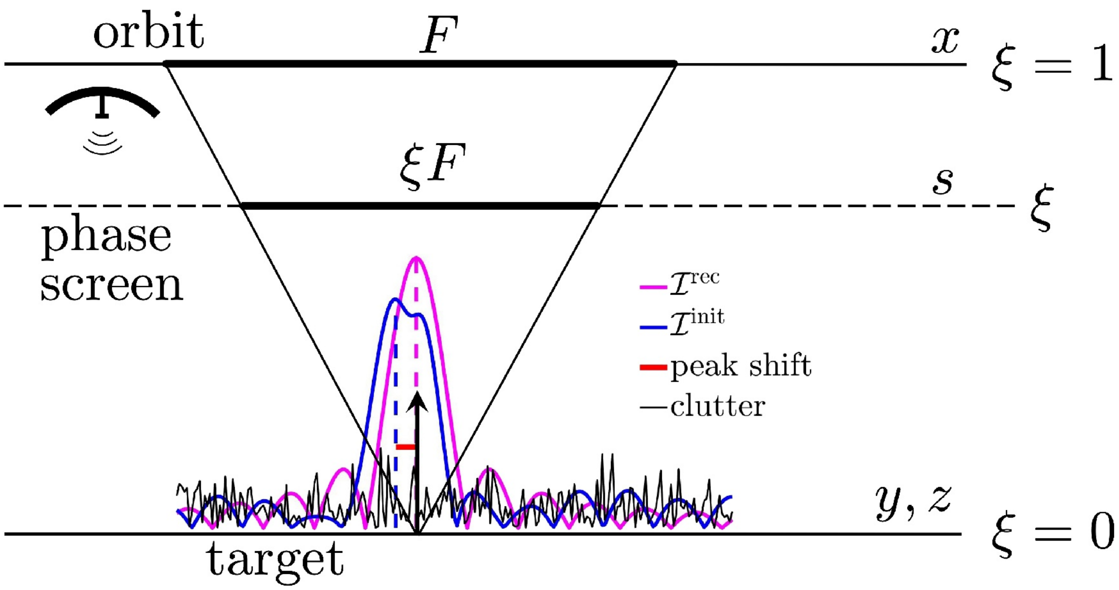

FIGURE 2 | Two-dimensional SAR geometry in a single slant plane with one-dimensional phase screen. Corrected (purple) and uncorrected (blue) SAR images due to a point scatterer (black arrow) and clutter are shown schematically.

that $0 < \xi < 1$, see Figure 2. Hence, in the range compressed domain, we will assume that the average phase velocity for each ray connecting $\boldsymbol{X}$ and $\boldsymbol{Z}$ is specified via a certain univariate dimensionless function $\Psi(S)$, where S is the coordinate of the intersection between this line and the ray.

The electron number density in the ionosphere $n_{\mathrm{e}}(\boldsymbol{r})$ that defines the phase and group velocities via Equation (4) consists of the background electron number density and turbulent fluctuations. As mentioned earlier, the effect of the background ionosphere on spaceborne SAR imaging can be mitigated with help of dual-carrier probing, see refs. [3, 4] and (ref. [5], Chapter 3). Hereafter, we will be focusing on the effect of ionospheric turbulence only. In accordance with Equation (4) and taking into account the phase screen representation of the ionosphere, we will use the following expression for the phase velocity:

$$\frac{v_{\mathrm{ph}}^{\mathrm{avg}}(\boldsymbol{X}, \boldsymbol{Z})}{c} = 1 + \frac{c}{2R\omega_0}\Psi(S), \tag{7}$$

where the phase screen density $\Psi(S)$ will be thought of as representing the turbulent fluctuations of the ionosphere. The two-way signal travel time will be given by

$$t_{\mathrm{ph}}(\boldsymbol{X}, \boldsymbol{Z}) = \frac{2|\boldsymbol{X} - \boldsymbol{Z}|}{v_{\mathrm{ph}}^{\mathrm{avg}}(\boldsymbol{X}, \boldsymbol{Z})}. \tag{8}$$

We will use the Pythagorean theorem to express $|\boldsymbol{X} - \boldsymbol{Z}|$ via the dimensionless coordinates x and z obtained by scaling X and Z, respectively, to the azimuthal resolution Δ_{A} [5, 8]:

$$x = \frac{X}{\Delta_{\mathrm{A}}}, \quad z = \frac{Z}{\Delta_{\mathrm{A}}}, \quad \text{where} \quad \Delta_A = \frac{\pi R c}{\omega_0 L_{\mathrm{SA}}}. \tag{9}$$

Assuming that $L_{SA} \ll R$, we have

$$|\boldsymbol{X} - \boldsymbol{Z}| = \sqrt{R^2 + (X - Z)^2} \approx R\left(1 + \frac{1}{2}\frac{\Delta_A^2}{R^2}(x - z)^2\right). \tag{10}$$

The factor in front of Ψ in Equation (7) is small because the carrier wavelength $\lambda = 2\pi c/\omega_0$ is much smaller than R. Hence, substituting Equations (7) and (10) into Equation (8) and linearising the result, for the phase in Equation (6) we obtain the following:

$$\omega_0\left(t_{\text{ph}}(\boldsymbol{X}, \boldsymbol{Z}) - 2R/c\right) \approx \frac{\pi}{F}(x - z)^2 - \Psi(S),$$

where $F = L_{SA}/\Delta_A \gg 1$ is the dimensionless aperture length. Using Equation (9) to transition from dimensional to dimensionless function arguments in Equation (6) and retaining other notations, we obtain the following:

$$u(x) = \int \nu(z)\exp\left[\frac{\mathrm{i}\pi}{F}(x - z)^2 - \mathrm{i}\Psi(s(x, z))\right]w_u(x - z)\,\mathrm{d}z, \tag{11}$$

where according to Figure 2,

$$s(x, z) = \xi x + (1 - \xi)z. \tag{12}$$

Integration limits in Equation (11) are defined by the window function w_u that represents the beam footprint and hence has a finite support. In this study, we will use rectangular window or Welch (parabolic) window, both having F as the support diameter:

$$w^{\text{rect}}(x) = \mathbf{1}_{|x| \le F/2}, \quad w^{\text{Welch}}(x) = w^{\text{rect}}(x)\left[1 - \left(2\frac{x}{F}\right)^2\right]. \tag{13}$$

The window $w^{\text{Welch}}(x)$ is then normalised by its mean for use in Equation (14).

For the signal in the form Equation (11), the following expression realises the approximate inversion w.r.t. the unknown reflectivity $\nu(z)$ yielding the SAR image:

$$\mathcal{I}(y; \Psi^{\text{rec}}) = \frac{1}{F}\int u(x)\exp\left[-\frac{\mathrm{i}\pi}{F}(x - y)^2 + \mathrm{i}\Psi^{\text{rec}}(s(x, y))\right] w_{\mathcal{I}}(x - y)\,\mathrm{d}x, \tag{14}$$

where $y = Y/\Delta_A$ is yet another dimensionless azimuthal coordinate, cf. Equation (9). The transform in Equation (14) is called matched filtering. The case of no ionosphere, $\Psi^{\text{rec}} = \Psi = 0$, corresponds to standard (i.e., undistorted) SAR imaging, where for the rectangular windows in Equations (11) and (14), the image of a point scatterer $\nu(z) = \delta(z - z_0)$ is given by $\mathcal{I}(y) = sinc(\pi(y - z_0))$, where $sinc v = (\sin v)/v$. This *sinc* function has a peak (central lobe) of semi-width 1 centred at $y = z_0$ (the semi-width is equal to Δ_A in the dimensional form, see Equation (9)). When the ionosphere is present, the best possible reconstruction in Equation (14) is achieved for $\Psi^{\text{rec}} = \Psi$. Then, as shown in ref. [9], the image of a point scatterer also has a peak centred at $y = z_0$ with semi-width close to 1, see Figure 2.

However, in the context of SAR imaging, the perturbation phase $\Psi(s)$ is generally not known, so a reconstruction phase $\Psi^{\text{rec}}(s)$ different from $\Psi(s)$ may need to be used in Equation (14).

In the absence of information about Ψ, the default option is to use $\Psi^{\text{rec}} \equiv 0$; however, if $\Psi(s)$ varies on the horizontal scale of ξF or smaller and the magnitude of these variations is of the order of π or larger, then the resulting uncompensated image $\mathcal{I}^{\text{init}} \equiv \mathcal{I}(y; 0)$ may appear noticeably distorted (in particular, the peak width may increase). The transionospheric autofocus algorithm of ref. [9] starts with $\mathcal{I}^{\text{init}}$ and improves it by varying Ψ^{rec}. The focusing is successful if Ψ^{rec} approximates Ψ with sufficient accuracy, resulting in a high-quality image $\mathcal{I}^{\text{rec}} \equiv \mathcal{I}(y, \Psi^{\text{rec}})$ where the effect of perturbations is minimised. The choice of the window function $w_{\mathcal{I}}$ in Equation (14) controls the image sidelobes [8]; one may take $w_{\mathcal{I}}$ the same as or different from w_u in Formula (11).

3 | Experimental Setup

3.1 | Definition of the Phase Screen

The Earth's ionosphere is a turbulent region where the electron number density $n_e(\boldsymbol{r})$, see Equation (4), experiences fluctuations characterised by inner and outer turbulence scales. Observations of free turbulence generally follow a power-law decay with respect to the spatial frequency, consistent with Kolmogorov's spectra of turbulence [21, 22]. Accordingly, the function $\Psi(s)$ that models the effect of the ionospheric turbulence on the signal propagation should be random. In our model, $\Psi(s)$ in Equation (11) is represented as a finite Fourier series:

$$\begin{aligned}\Psi(s) &= \operatorname{Re}\sum_{n=1}^{N} a_n \exp\left(\mathrm{i}k_n s + \mathrm{i}\varphi_n\right) \\ &= \sum_{n=1}^{N}(p_n \cos(k_n s) + q_n \sin(k_n s)),\end{aligned} \tag{15}$$

such that

$$p_n = a_n \cos(\varphi_n), \quad q_n = -a_n \sin(\varphi_n).$$

In Equation (15), N is the number of harmonics, a_n are the real-valued amplitudes of the harmonics, and k_n represents the wavenumber of the n^{th} harmonic. To specify the spatial spectrum of Ψ, we first define the fundamental scale as a multiple of the (dimensionless) synthetic aperture length: $l_z = \rho F$. The fundamental wavenumber is $k_1 = 2\pi/l_z$, and each spatial frequency in the spectrum of Ψ is an integer multiple of this fundamental frequency:

$$k_n = nk_1 \equiv \frac{2\pi}{\rho F}n, \quad n = 1, 2, \ldots, N. \tag{16}$$

Short- and long-scale models correspond to $\rho \lesssim 1$, and $\rho \gtrsim 1$, respectively. The perturbation effects tend to decrease as ρ increases, see ref. [15]. In this work, we use a medium-scale model with $\rho = 5/3$, an arbitrary choice that establishes a baseline scenario where autofocusing is effective. Note that the wavenumbers k_n need not necessarily be integer multiples of the fundamental wavenumber as in Equation (16), that is, there is no physical requirement for periodicity in Ψ. Still, we choose to make Ψ periodic for the purposes of this study.

The randomness in Equation (15) is realised by φ_n that are taken as independent uniformly distributed $\left(\varphi_n \sim \mathcal{U}[-\pi, \pi]\right)$ phase shifts. While the amplitudes $\{a_n\}_{n=1}^{N}$ in Equation (15) adhere to a power-law decay to reflect the energy dissipation at higher spatial frequencies, the randomised phases φ_n allow the model to generate multiple realisations of the phase screen with identical spectral properties.

Note that if $\Psi(s)$ were linear in s, then for $\Psi^{\mathrm{rec}} \equiv 0$ the peak due to a point scatterer in the resulting image $\mathcal{I}^{\mathrm{init}}$ will be shifted with respect to the position of the scatterer, see Appendix B. The model Equation (15) with a relatively small N cannot adequately represent a linear function. However, as ρ increases, the leading harmonic (which has also the largest amplitude) behaves approximately linearly on the intervals of s with the length of ξF (see Figure 2), leading to a shift of the corresponding part of the image. Variation of this effect over the image produces geometric distortions.

The magnitude of the screen density function, later referred to as Ψ-magnitude, is defined as follows:

$$\|\Psi\| \equiv \|\Psi\|_2 = \left(\sum_{n=1}^{N} |a_n|^2\right)^{1/2}. \qquad (17)$$

A notable observation in ref. [9] was that achieving an effective autofocus becomes more complicated as $\|\Psi\|$ increases. A comparison of autofocusing outcomes for $\|\Psi\| = 2\pi$ and $\|\Psi\| = 7\pi$, see Figure 3, demonstrates the deterioration in autofocusing efficacy for large $\|\Psi\|$.

For this study, we build upon a baseline example from previous work [9]. In particular, we use $N = 6$, $F = 100$, and $\rho = 5/3$ in formulae (15) and (16). The set $\{a_n\}_{n=1}^{6}$ corresponding to $\|\Psi\| = 2\pi$ is presented in Table 1 (it follows a quadratic power law as in ref. [9]). For our statistical autofocus analysis, we simulate ensembles of ionospheric phase screens by randomly sampling the sets of phase shifts $\{\varphi_n\}_{n=1}^{6}$ and substituting the result into Equation (15).

3.2 | Discretisation and Point Scatterers

In addition to the parameters mentioned in Section 3.1, we specify the grid discretisation size $\delta_x = 0.25$ for x, y, and z in order to calculate the quadratures in formulae (11) and (14), and choose $\xi = 0.5$. The spatial domain for the target reflectivity ranges from $z = 0$ to $z = 360$. Since the support of the window functions Equation (13) used in Equations (11) and

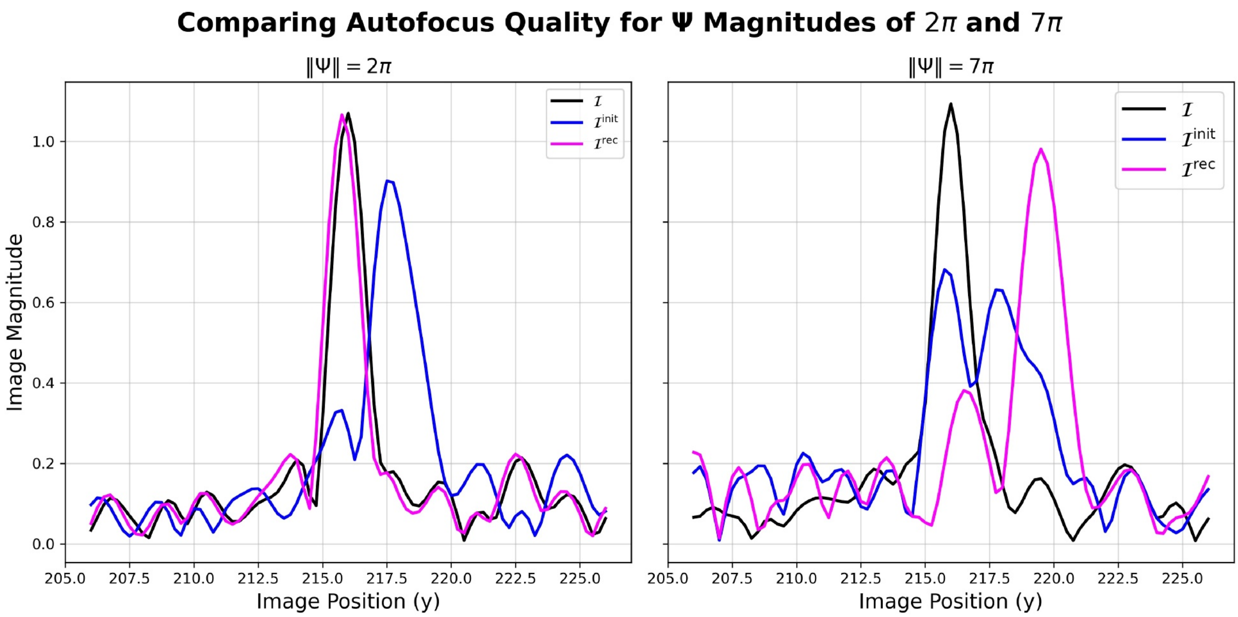

FIGURE 3 | Comparison of two autofocusing scenarios with different perturbation levels: $\|\Psi\| = 2\pi$ (left) and $\|\Psi\| = 7\pi$ (right).

TABLE 1 | Parameters of the baseline amplitude spectrum of the screen density function corresponding to $N = 6$, $F = 100$, and $\rho = 5/3$, see Equations (15) and (16).

	$n = 1$	$n = 2$	$n = 3$	$n = 4$	$n = 5$	$n = 6$
Real amplitudes (a_n)	6.0428	1.5107	0.6714	0.3776	0.2417	0.1678
Wavenumbers (k_n)	0.0377	0.0754	0.1131	0.1508	0.1885	0.2262

(14) has the diameter of $F = 100$, the signal $u(x)$ and image $\mathcal{I}(y)$ are defined in the domains $x \in [50, 310]$ and $y \in [100, 260]$, respectively. We specify three point scatterers, each of unit magnitude, located at $z_1 = 144$, $z_2 = 186$, and $z_3 = 216$, that is, all three resulting peaks should show up in the SAR images. This defines the deterministic part of the reflectivity function as follows:

$$\nu_{\mathrm{PS}}(z) = \sum_{i=1}^{3} \delta(z - z_i). \tag{18}$$

3.3 | Clutter

Clutter refers to the unwanted backscattering that occurs near the 'useful' targets. Whereas in our model, the latter are specified as high-reflectivity point scatterers, clutter will be represented by a random grid function added to ν_{PS} given by Equation (18). We consider $\nu_{\mathrm{clutter}}(z)$ to be complex valued, and the real (X_{C}) and imaginary (Y_{C}) components of each point on the target domain are independent, normally distributed with identical variance. In order to relate the average level of reflectivity to that of the prominent point scatterers, we use the Rayleigh distribution where the variance of the normally distributed real and imaginary components are

$$\sigma^2 = \sigma_{\mathrm{C}}^2 \frac{2}{\pi}$$

Such that the mean reflectivity of the clutter on the target domain is $\mathbb{E}(|X_{\mathrm{C}} + iY_{\mathrm{C}}|) = \sigma_{\mathrm{C}}$:

$$\nu_{\mathrm{clutter}} = \sqrt{\delta_x}[X_{\mathrm{C}} + iY_{\mathrm{C}}], \quad \text{where } X_{\mathrm{C}}, Y_{\mathrm{C}} \sim \mathcal{N}\left(0, \frac{2\sigma_{\mathrm{C}}^2}{\pi}\right). \tag{19}$$

In Equation (19), the length of the random vectors X_{C} and Y_{C} is consistent with the length of the target domain. The total target reflectivity $\nu(z)$ in Equation (11) will then be given as follows:

$$\nu(z) = \nu_{\mathrm{PS}}(z) + \nu_{\mathrm{clutter}}(z), \tag{20}$$

with the terms of the right-hand side of (20) defined in Equations (18) and (19). In other words, we consider the average level of reflectivity $\sigma_{\mathrm{C}} \in [0.009, 0.177]$, relative to the reflectivity of $|\nu_{\mathrm{PS}}| = 1$. [1]

The choice for the range of the clutter intensity σ_{C}^2 in Equation (19) is supported by an example from NASA/JPL UAVSAR database. On the left panel in Figure 4, we provide an L-band, single look complex (SLC) SAR image showing the Los Angeles Basin with a mixture of urban and mountainous terrain with several bodies of water. There are well-defined point scatterers

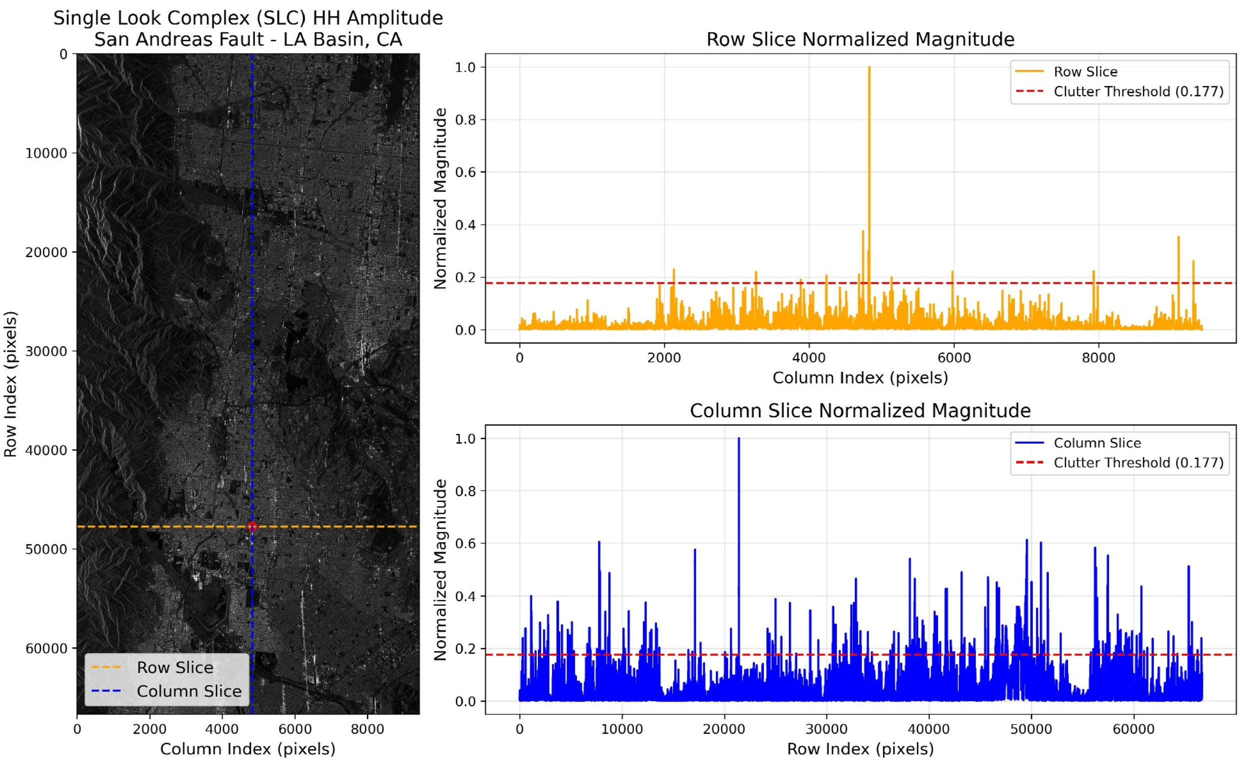

FIGURE 4 | An L-band single look complex (SLC) SAR image of the San Andreas Fault/Los Angeles Basin from NASA/JPL's UAVSAR database. The image, composed of approximately 628 million complex-valued pixels, is linearly scaled with an intensity cutoff at the 99$^{\mathrm{th}}$ percentile of pixel magnitudes. A point in the image was selected based on yielding a prominent magnitude of reflectivity as well as there being a mixture of different terrains in the row and column slices: urban, mountainous, and bodies of water. For the row and column slices, the mean amplitude of clutter relative to the most prominent point scatter is 0.019 and 0.033, respectively. Acquisition details: NASA UAVSAR, L-band ($\lambda = 23.84cm$), polarisation: HH, flight line ID: 26,524.

in this image. We find high intensity point scatterers in the image, take the corresponding column and row slices, and plot the intensities along these slices on the right panels in the same figure. These plots show that 0.177 is a reasonable upper bound level of average clutter reflectivity. Note that typically, long-wavelength radar missions are designed for forest and ice applications where point scatterers are not abundant.

3.4 | Noise

Noise represents the inherent randomness that distorts the waveform, originating from instrumental limitations, environmental factors, and interference from external signals. For consistency in comparing the sensitivity of clutter and noise, we chose a range of noise levels as $\sigma_{\mathrm{N}} \in [0.009, 0.177]$. Here, σ_{N} denotes the expected level of noise as a fraction of the maximum magnitude of the useful signal $u_{\mathrm{clean}}(x)$. Similar to Section 3.3, we generate independent normal random vectors with zero mean and variance $\sigma^2 = \sigma_{\mathrm{N}}^2(2/\pi)$.

$$X_{\mathrm{N}}, Y_{\mathrm{N}} \sim \mathcal{N}\left(0, \frac{2\sigma_{\mathrm{N}}^2}{\pi}\right) \tag{21}$$

of appropriate length and define

$$u_{\mathrm{noise}}(x) = \max_x(|u_{\mathrm{clean}}(x)|) \cdot [X_{\mathrm{N}} + \mathrm{i}\ Y_{\mathrm{N}}], \tag{22}$$

where the noise-free signal $u_{\mathrm{clean}}(x)$ is the output of Equation (11). The total signal $u(x)$ to be substituted into Equation (14) is calculated as follows:

$$u(x) = u_{\mathrm{clean}}(x) + u_{\mathrm{noise}}(x). \tag{23}$$

3.5 | Cost Function

Our autofocus algorithm seeks to minimise the following cost function:

$$\begin{aligned}\mathrm{Cost}(\mathbf{p}^{\mathrm{rec}}, \mathbf{q}^{\mathrm{rec}}) = &-\delta_x \sum_i |\mathcal{I}(y_i; \Psi^{\mathrm{rec}}(\cdot\,; \mathbf{p}^{\mathrm{rec}}, \mathbf{q}^{\mathrm{rec}}))|^4 \\ &+\zeta \sum_{n=1}^{N} k_n^2\left(\left(p_n^{\mathrm{rec}}\right)^2 + \left(q_n^{\mathrm{rec}}\right)^2\right).\end{aligned} \tag{24}$$

The first term of the cost function is built using the fourth power of the ℓ_4 norm of the SAR image. Its minimisation leads to sharpening of the peaks [23, 24], whereas the scaling with δ_x provides consistency for different grid sizes. The second term, weighted by the constant ζ, serves as a regularisation: it penalises high-amplitude oscillations of Ψ on small spatial scales. The vectors $\mathbf{p}^{\mathrm{rec}}$ and $\mathbf{q}^{\mathrm{rec}}$ composed of the Fourier amplitudes p_n^{rec} and q_n^{rec}, see Equation (15), serve as the control variables. The value of $\zeta = 0.6$ was chosen based on the consistency and quality of the focused images compared to the true images in the corresponding scenarios, see the discussion around Figure 5.

3.6 | Optimisation Process

Our goal is to produce a SAR image $\mathcal{I}^{\mathrm{rec}} \equiv \mathcal{I}(y; \Psi^{\mathrm{rec}})$ that would yield the best possible approximation of the ideal reconstruction image $\mathcal{I}(y; \Psi)$. We hypothesise that this can be achieved by minimising the cost function (24). For a given reflectivity function $\nu(z)$ and fixed noise level, the value of $|\mathcal{I}(y, \cdot)|$ given by Equations (11), (14), and (22) is bounded for every y, while the second term on the right hand side of Equation (24) is positive semidefinite. Thus, $\mathrm{Cost}(\mathbf{p}^{\mathrm{rec}}, \mathbf{q}^{\mathrm{rec}})$ is bounded from below. Moreover, smoothness of the cost function with respect to the control variables can be seen from the analytic form of Equations (14), (15), and (24), see also Appendix (A). Hence, the gradient descent is guaranteed to converge to a local minimum.

To perform the optimisation, we employ a gradient-based method to minimise the cost function specified in (24). The calculation of the gradient is detailed in Appendix A. We use the Python implementation of Broyden-Fletcher-Goldfarb-Shanno (BFGS) quasi-Newton method. This method is a popular choice for multidimensional minimisation problems because it approximates the Hessian matrix of the cost function without directly computing the second derivatives. We specify the stopping condition in the BFGS implementation of `scipy.optimise.minimise` as $||\nabla\ \mathrm{Cost}|| < 0.001$.

4 | Outline of the Study

In this work, we conduct a statistical study of the effectiveness of SAR autofocus [9] when applied to a phase-perturbed signal with perturbations induced by ionospheric effects. We vary three parameters independently to observe their individual impacts:

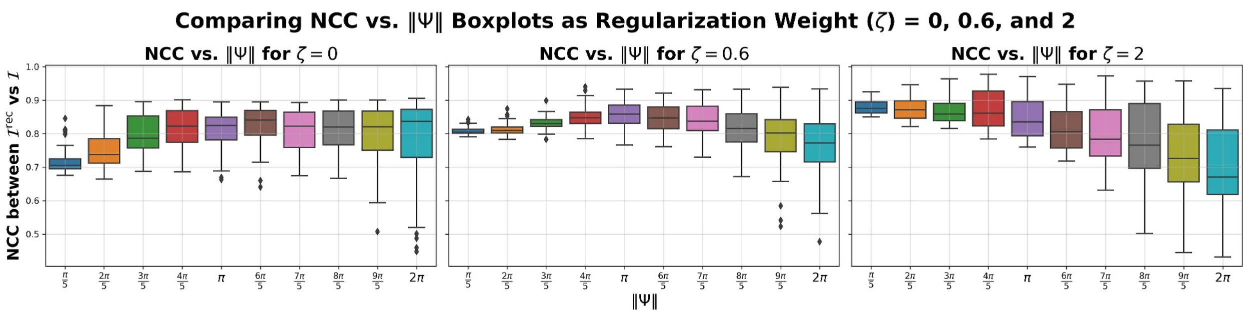

FIGURE 5 | Comparison of NCC versus $||\Psi||$ for regularisation weights $\zeta = 0$, 0.6, and 2. The middle panel ($\zeta = 0.6$) corresponds to Figure 6.

- The magnitude of phase perturbation (Ψ-magnitude) given by Equation (17).
- The average reflectivity of the ground clutter, σ_C, see Equation (19).
- The mean level of the antenna noise, σ_N, see Equation (21).

These three parameters were chosen because they represent and control the key sources of stochasticity in the formulation, as detailed in Section 3. Variations in the phase shifts, clutter reflectivity, and noise introduce randomness into the system, which in turn influences the values of metrics that assess the quality of the focused image. By modelling these sources of stochasticity, we can evaluate the robustness of the autofocus algorithm.

5 | Results

5.1 | Quality of Focusing Versus Level of Perturbations

We employed the normalised cross-correlation (NCC) of image magnitude as a primary metric to quantitatively assess the similarity between the autofocused and true images. We calculate NCC using the following formula:

$$\mathrm{NCC}(\mathcal{I},\mathcal{I}^{\mathrm{rec}};\mu)=\max_{\nu\in[-\mu,\mu]}\frac{\sum_i(|\mathcal{I}(y_i)|-\mathrm{mean}(|\mathcal{I}|))(|\mathcal{I}^{\mathrm{rec}}(y_i-\nu)|-\mathrm{mean}(|\mathcal{I}^{\mathrm{rec}}|))}{\sqrt{\sum_j(|\mathcal{I}(y_j)|-\mathrm{mean}(|\mathcal{I}|))^2\sum_k(|\mathcal{I}^{\mathrm{rec}}(y_k-\nu)|-\mathrm{mean}(|\mathcal{I}^{\mathrm{rec}}|))^2}}. \quad (25)$$

Here, $\mathrm{mean}(|\mathcal{I}^{\mathrm{rec}}|)$ and $\mathrm{mean}(|\mathcal{I}|)$ represent the magnitudes of the reconstructed, that is, autofocused image $\mathcal{I}^{\mathrm{rec}}\equiv\mathcal{I}(y;\Psi^{\mathrm{rec}})$ and 'true' image $\mathcal{I}\equiv\mathcal{I}(y;\Psi)$, respectively, averaged over the spatial coordinates. Since the cost function (24) is almost insensitive to a shift of the image as a whole, the NCC is evaluated at its maximum over the allowable interval of shifts of the reconstructed image. In particular, we allow the shift ν in Equation (25) to vary in the interval $[-\mu,\mu]$ and set $\mu=10$ to account for the cases where $\mathcal{I}^{\mathrm{rec}}$ closely resembles a shifted version of $\mathcal{I}$. In our tests, the shifts of the peaks in $\mathcal{I}^{\mathrm{rec}}$ are consistently within this range, ensuring $(1-\mathrm{NCC})\ll 1$ for highly coherent, albeit shifted images.

In our first set of numerical experiments, we choose 10 equidistant values of Ψ-magnitude, see Equation (17), between $\pi/5$ to 2π. This range covers a significant part of observable levels of ionospheric perturbation, see (ref. [9], Appendix A). For each of these 10 values of $\|\Psi\|$, we generate 100 realisations of the screen density function $\Psi(s)$ according to a procedure described in Section 3.1. The variability in the autofocus performance originates from the difference between the realisations of $\Psi(s)$ defined by the sets of phase shifts $\{\varphi_n, n=1,\ldots,6\}$ via Formula (15). Other simulation parameters correspond to the baseline scenario described in Section 3.1.

Table 2 and Figure 6 provide an overview of the results of this simulation. For a baseline level of clutter $\sigma_C=0.089$ and noise $\sigma_N=0.044$, we see that the autofocus algorithm maintains a certain degree of robustness across all perturbation levels. The overall median NCC across all levels of ionospheric turbulence, $|\Psi|$, is 0.82. For realisations where $|\Psi|\le\pi$, the median NCC is 0.82, whereas for $|\Psi|>\pi$, it slightly decreases to 0.81. The highest autofocusing performance achieved an NCC of 0.94 at $|\Psi|=\frac{4\pi}{5}$, while the lowest performance yielded an NCC of 0.45 at $|\Psi|=2\pi$. Figure 6 further illustrates the statistics of the optimisation outcomes by showing the quartile values for each level of Ψ-magnitude. Although the median NCC remains stable across different turbulence levels, the variance in NCC noticeably increases with higher ionospheric turbulence. Several outliers with relatively low values of NCC will be analysed in Section 5.2.

The increasing share of lower NCC values for larger magnitudes of Ψ observed in Figure 6 indicates a deterioration of focusing capacity of the autofocus algorithm. This behaviour is expected for higher levels of turbulence. Yet what we also see in Figure 6 is a slight degradation of focusing toward lower values of $\|\Psi\|$, as manifested by the decrease of the median NCC accompanied by the decrease of variance (the latter showing a tighter grouping of the results). We attribute this behaviour to the effect of clutter which still pertains even for low levels of turbulence. Indeed, for the ultimate scenario with no perturbations at all, $\Psi=0$, we would expect to reconstruct $\Psi^{\mathrm{rec}}=0$. This is obvious, because if there is no turbulence, then there are no turbulence-induced distortions, and no improvement of focusing is needed. Likewise, for low magnitudes of Ψ, we would expect the reconstructed screen density Ψ^{rec} to be commensurately small. However, a fixed level of clutter (and noise) affects the resulting optimal solution, because the algorithm essentially tries to focus up the areas of clutter and noise. Yet with clutter being a high-frequency phenomenon and Ψ and Ψ^{rec} represented on much lower frequencies, convergence of the optimiser in this low-frequency subspace does not ameliorate the clutter but makes the focusing slightly worse, because ideally little to no correction would be required.

In addition, we have investigated how the penalty weight ζ in the definition of the cost function (24) affects the behaviour of NCC as a function of $\|\Psi\|$. The penalty term promotes the decrease of the amplitudes of individual harmonics in the spectrum of Ψ^{rec} with the increase of their frequency; however, this term also favours small over large values of $\|\Psi^{\mathrm{rec}}\|$ in general. Hence, with no penalty ($\zeta = 0$) we observe a more stable behaviour of the median NCC for higher $||\Psi||$ yet with a considerable variance, and a somewhat stronger deterioration for lower $||\Psi||$, see the left panel in Figure 5. On the other hand, for high penalty ($\zeta = 2$) the dependence of NCC on $||\Psi||$ basically becomes monotonic, but the degradation of performance for higher $||\Psi||$ appears more substantial, see the right panel in Figure 5. The middle panel in Figure 5 ($\zeta = 0.6$) corresponds to Figure 6. It strikes an efficient balance, showing solid performance with a fairly low variance for all levels of Ψ magnitude. The value of $\zeta = 0.6$ is used in all subsequent simulations.

Figures 7 and 8 show the impact of clutter and noise varying in the range from 0.009 to 0.177 on NCC. While ionospheric turbulence and clutter are distinct phenomena—thus making direct comparisons challenging—our analysis employs realistic, predetermined levels for both. At higher clutter levels, we observe a more pronounced decline in the median NCC in Figure 7 as compared to the modest declines caused by large Ψ-magnitudes in Figure 6. The median NCC drops from 0.85 for low clutter ($\sigma_C \leq 0.1$) to 0.59 for high clutter ($\sigma_C > 0.1$). Notably, 26% of low-clutter cases achieve NCC $\geq$0.9, whereas only 1.1% of the high-clutter cases do, and over 87% of the high-clutter cases fall below 0.8. The best NCC of 0.98 occurs at $\sigma_C = 0.08$, while the worst is 0.30 at $\sigma_C = 0.17$. This suggests that while autofocusing effectively reconstructs scatterer intensities and positions, increased clutter degrades correlation due to additional reflectivity in the off-peak areas.

TABLE 2 | Rows 2 to 11 correspond to 10 equidistant levels of Ψ-magnitude ranging from $\pi/5$ to 2π. Columns 2 through 4 represent the number of realisations (out of 100 for each level) where an NCC value above or equal to the specified threshold has been achieved.

Ψ magnitude	**Cases (NCC ≥ 0.85)**	**Cases (NCC ≥ 0.8)**	**Cases (NCC ≥ 0.75)**
$\pi/5$	0	36	100
$2\pi/5$	2	59	100
$3\pi/5$	10	92	100
$4\pi/5$	36	96	100
π	54	88	100
$6\pi/5$	41	81	100
$7\pi/5$	36	76	97
$8\pi/5$	27	54	80
$9\pi/5$	24	46	68
2π	19	35	53

On the other hand, Figure 8 shows that the autofocus algorithm is notably more robust in the presence of high noise levels (σ_N), with a median NCC of 0.92, compared to its sensitivity to ionospheric turbulence and clutter. The best performance reaches an NCC of 0.97, while the worst drops to 0.76. Only 2 scenarios fall below NCC = 0.8, indicating that noise has a minimal impact on image quality compared to clutter. This is not surprizing because noise (22) is modelled as an additive zero-mean Gaussian term to the antenna signal $u(x)$, and due to the integration in Equation (14), its influence is averaged out.

5.2 | Worst-Case Scenarios and Additional Distortion Metrics

One of the rhombus-shaped dots at $||\Psi|| = 2\pi$ in Figure 6 indicates an outlier with NCC $\approx$ 0.45. Figure 9 visualises this worst-case scenario, demonstrating that the autofocus algorithm may degrade the image quality with regard to the peak locations and NCC despite yielding a lower cost function. Our autofocused image, $\mathcal{I}^{\mathrm{rec}}$, shows a narrowing of peaks, but there

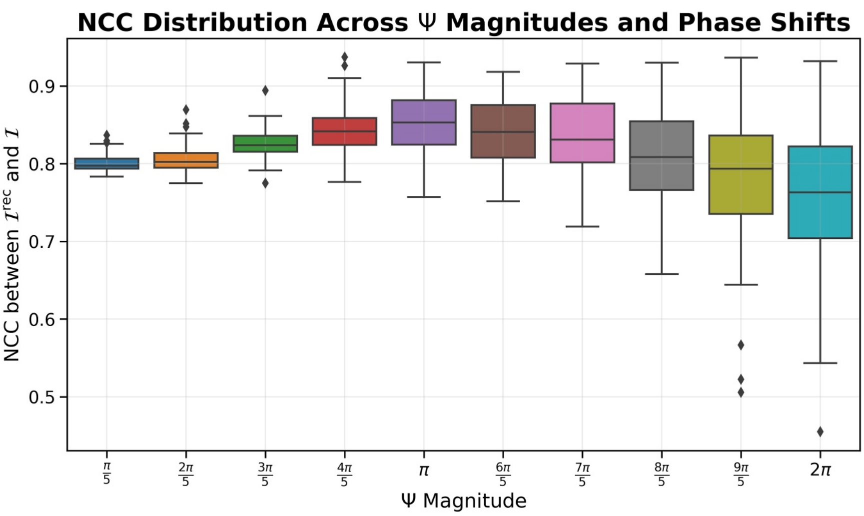

FIGURE 6 | Normalised cross-correlation (NCC) across 100 realisations for each of 10 equally spaced bins of Ψ-magnitude visualised using box plots. Each coloured box represents the middle 50% of the data (also called the interquartile range, or IQR), with whiskers extending to the most extreme data points within 1.5 times the IQR from the quartiles. Outliers are shown as individual rhombus-shaped points outside of these bounds, see Section 5.2. The nonmonotonic behaviour of NCC is analysed in Figure 5 and the associated discussion.

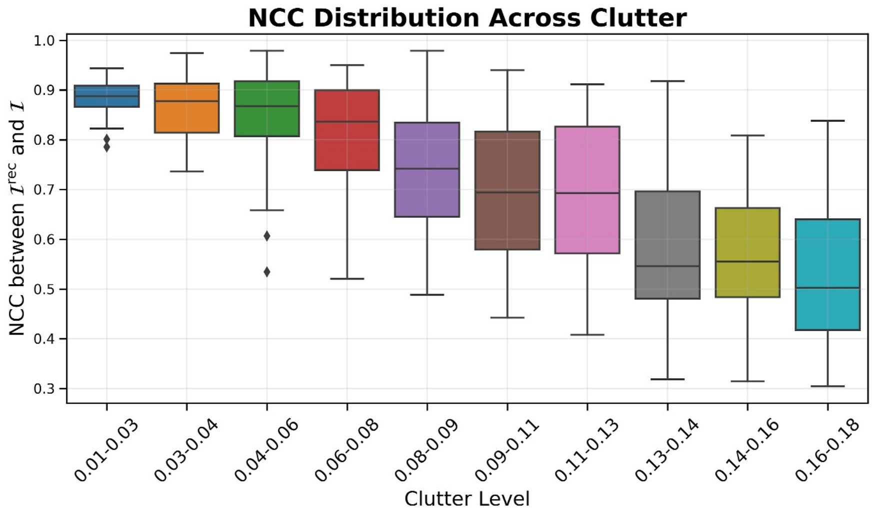

FIGURE 7 | Same as in Figure 6, but for varying levels of σ_{C}.

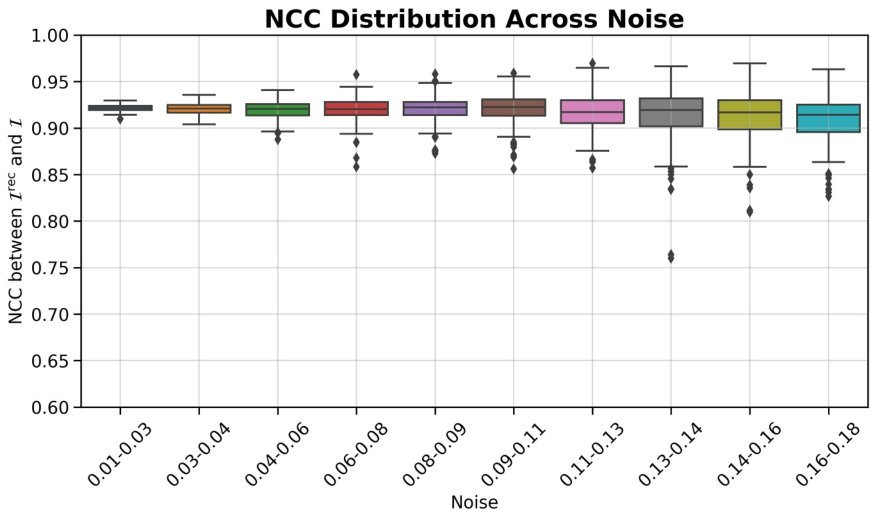

FIGURE 8 | Same as in Figure 6, but for varying levels of σ_{N}.

is a notable decline in image quality from the initial image, $\mathcal{I}^{\mathrm{init}}$, to $\mathcal{I}^{\mathrm{rec}}$. We employ a multi-start global optimisation scheme which sends out 384 optimisation agents in a constrained search domain, and each agent locally optimises to its minimum based on its initial placement; from all workers, we select the lowest one as our multi-start global minimum. In Figure 9, we see an image improvement from the multi-start, autofocused image, $\mathcal{I}^{\mathrm{multi}}$, compared to $\mathcal{I}^{\mathrm{init}}$ and $\mathcal{I}^{\mathrm{rec}}$. This provides evidence that the zero-initialised, single optimiser which generates $\mathcal{I}^{\mathrm{rec}}$ and the bulk of the figures and data in this paper, can converge to suboptimal (local) minima where the autofocused image quality is not significantly improved as compared to that of $\mathcal{I}^{\mathrm{init}}$.

However, we can see that the displacement of the peaks in $\mathcal{I}^{\mathrm{multi}}$ does not amount to a shift of the image as a whole because one of the peaks is shifted in the direction opposite to that of the other two peaks. Although the peaks in the resulting image are sharp and their heights are on par with those of the true image, we still consider such image as geometrically distorted, with one part stretched and another compressed compared to the ground truth. For this reason, we consider this behaviour of NCC as a distortion metric appropriate.

To quantitatively assess the geometrical distortion described above, we introduce the concept of peak desynchronisation (PD) as a measure of variation in the peak shifts between the autofocused and true images:

$$\mathrm{PD}(\mathcal{I}, \mathcal{I}^{\mathrm{rec}}) = std\left(\left\{y_p^{\mathrm{rec}} - y_p | p = 1, \ldots, N_{\mathrm{peaks}}\right\}\right), \qquad (26)$$

where std denotes standard deviation, y_p and y_p^{rec} are the ordered peak locations in $\mathcal{I}$ and $\mathcal{I}^{\mathrm{rec}}$, respectively, and N_{peaks} is the total number of peaks (in this case, $N_{\mathrm{peaks}} = 3$). Such a metric reflects the degree of nonuniformity in the image shift induced by the phase screen. A PD value of zero indicates a perfect shift of the set of peaks as a whole, including the case of no shift at all.

Figure 10 presents a close-up of the worst-case scenario in Figure 7. Unlike in Figure 9, we see a significant increase of

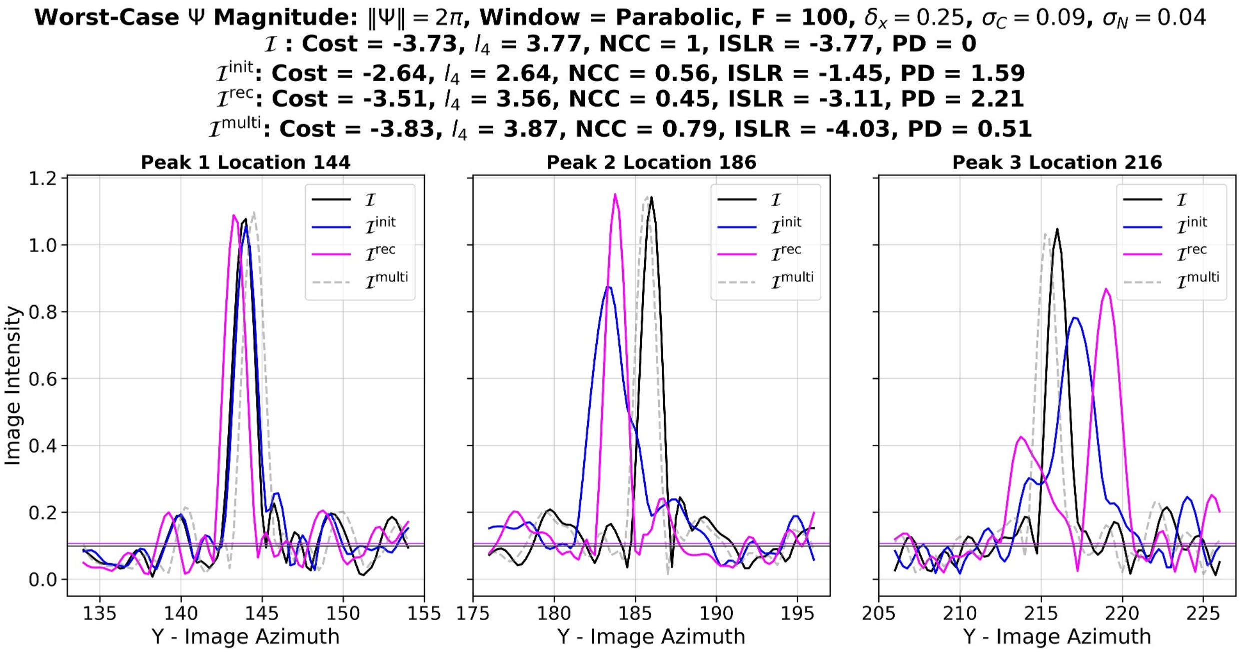

FIGURE 9 | The worst-case scenario for Figure 6. The single optimiser initialised at zero amplitudes (magenta) fails to improve image quality, reducing NCC to 0.45 and increasing PD to 2.21, despite improving ISLR given by (27) from -1.45 dB to -3.11 dB. In contrast, the multi-start method (grey dashes) produces an image that is very close to the true image (black), achieving an NCC of 0.79, ISLR of -4.03 dB, and significantly reduced PD of 0.51.

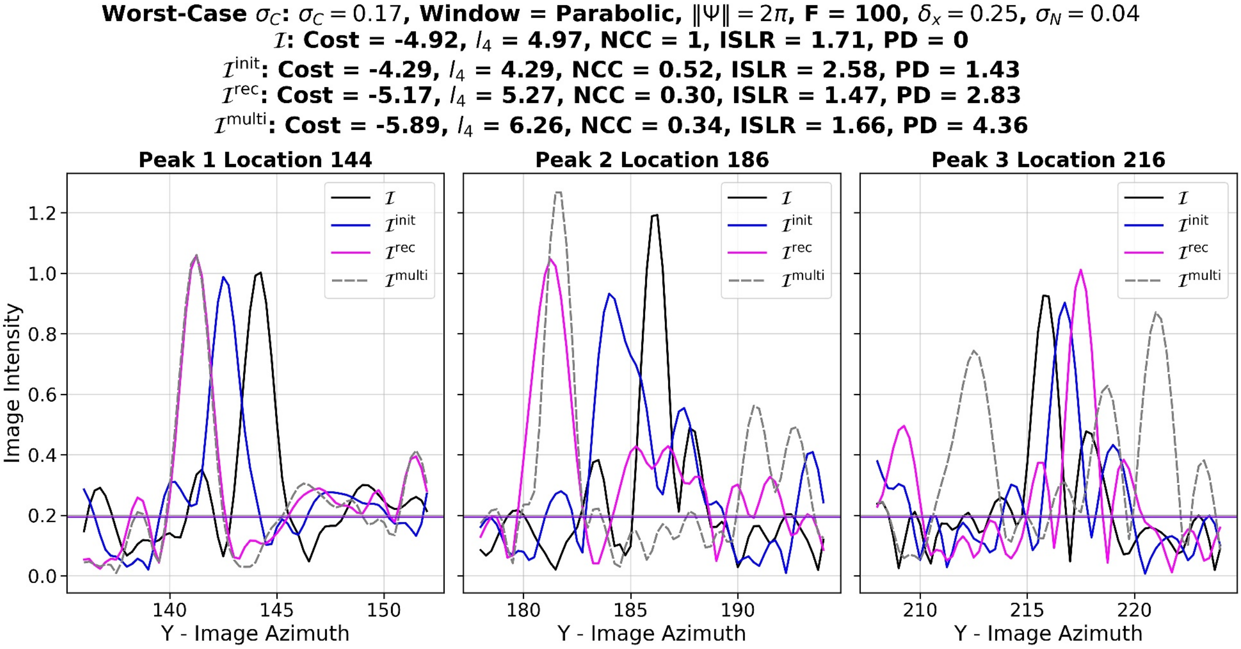

FIGURE 10 | The worst-case scenario for Figure 7. Both the single optimiser initialised at zero amplitudes ($\mathcal{I}^{\text{rec}}$, magenta) and the multi-start optimiser ($\mathcal{I}^{\text{multi}}$, grey dashes) failed to recover the true image ($\mathcal{I}$, black), despite converging to cost function minima. While peak sharpening is observed (ISLR improves from 2.58 to 1.47 dB for $\mathcal{I}^{\text{rec}}$), severe peak desynchronisation (PD increases to 2.83) undermines autofocus performance. The high sidelobe energy in $\mathcal{I}$ (ISLR = 1.71 dB) highlights the challenge clutter poses for autofocus, with the sidelobes containing as much energy as the main peaks.

sidelobes in the focused image and reduction of peak heights in addition to PD. In order to quantify this kind of distortions, we compute the integrated sidelobe ratio (ISLR) that characterises peak prominence relative to sidelobes. ISLR is calculated according to the following formula (ref. [8], Section 2.8):

$$\mathrm{ISLR} = 10\log_{10}\left(\frac{E_{\text{sidelobes}}}{E_{\text{peaks}}}\right), \tag{27}$$

where

$$E_{\text{peaks}} = \sum_{p}^{N_{\text{peaks}}} \int_{\{y:|y-y_p|\le 1\}} |\mathcal{I}^{\text{rec}}(y)|^2\, dy,$$
$$E_{\text{sidelobes}} = \left(\sum_{p}^{N_{\text{peaks}}} \int_{\{y:|y-y_p|\le \mu_{\text{peak}}\}} |\mathcal{I}^{\text{rec}}(y)|^2\, dy\right) - E_{\text{peaks}} \tag{28}$$

In Equation (28), we use $\mu_{\text{peak}} = 20$, which is smaller than the distance between the peaks. We observe that unlike in Figure 9, the ISLR value calculated for the reconstructed image is significantly higher than that of the true image. This degradation in image quality may be attributed to the optimiser that, always initialised at zero amplitudes, may settle at a local rather than global minimum of the cost function. We see that this is actually the case in Figure 10, as well as in Figure 9.

Different metrics of focusing quality used in this work complement each other and are sensitive to different kinds of image distortions. As an example, Figure 11 illustrates the behaviour of PD and NCC for different levels of clutter. We see that a decrease in PD is not always equivalent to an increase in NCC. This figure also contrasts the true perturbation $\Psi(s)$ with $\Psi^{\text{rec}}(s)$ obtained via the cost minimisation, and we observe an increase of discrepancy between the two with the increase of clutter level σ_C.

Let us also note that while the performance metrics such as PD defined by Equation (26) or ISLR defined by Equations (27)–(28) are very useful in that they help distinguish between efficient and inefficient focusing, they cannot be easily incorporated into the optimisation cost function. Indeed, the peak location can be a discontinuous function of the control variables $(\mathbf{p}^{\text{rec}}, \mathbf{q}^{\text{rec}})$. Therefore, smoothness of a peak-related cost function could not be guaranteed, which would make solving the resulting optimisation problem a lot more difficult. As such, we use the sparsity promoting yet smooth cost function (24) for optimisation and employ the peak-related metrics in the capacity of a posteriori performance indicators.

5.3 | Parameter Importance Ranking

Figure 11 suggests that besides the level of perturbations, other factors may significantly affect the quality of focusing. In addition to the levels of clutter and perturbation, we are interested in evaluating the effect of noise, as well as the phase shifts of individual harmonics in the Fourier representation of the screen density function, see Equation (15). Direct comparison of the effects of these parameters on NCC can be challenging because high levels of clutter lead to NCC degradation, even with a perfect reconstruction of the peaks. For this reason, in order to assess the impact of various factors on distortions in reconstructed images, we performed a mutual information (MI) analysis with peak desynchronisation (PD) as the primary distortion metric.

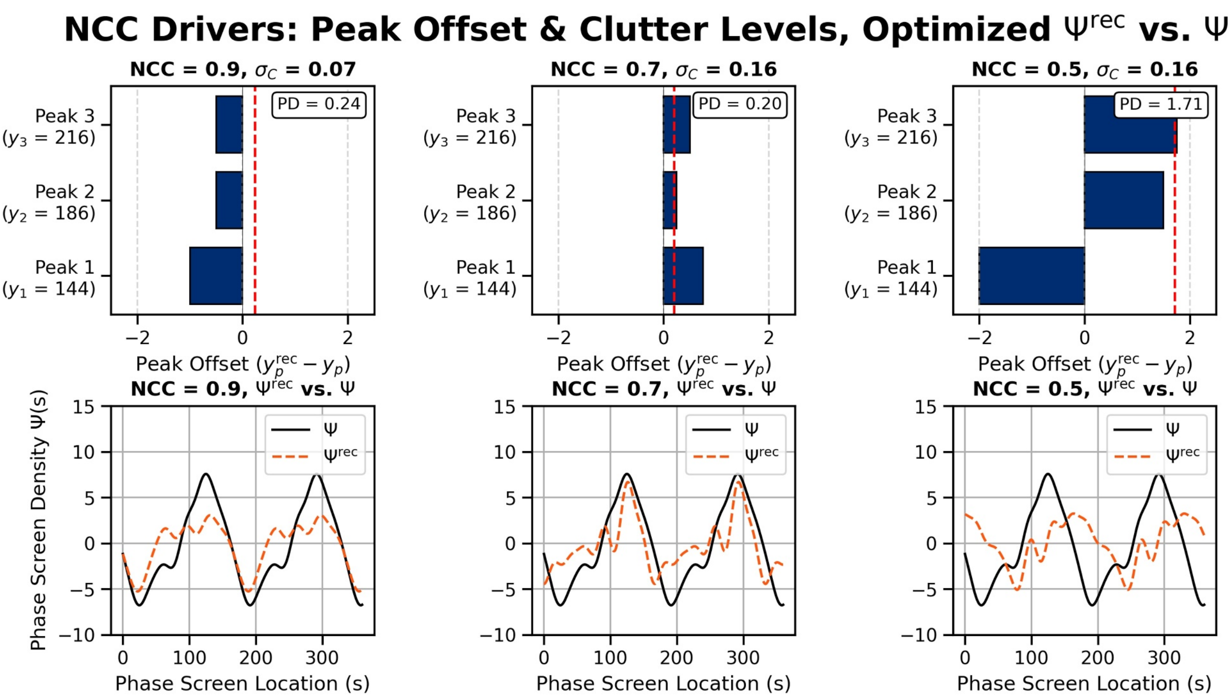

FIGURE 11 | Comparison of two primary factors affecting NCC: shifts of the peaks and the level of clutter. The three columns correspond to NCC levels of approximately 0.9, 0.7, and 0.5, respectively. The top row shows that as the peak locations of $\mathcal{I}^{\text{rec}}$ deviate from those in $\mathcal{I}$ and the clutter level increases, the NCC metric declines. The red dotted line represents the value of peak desynchronisation (PD). The bottom row displays the resulting phase screen density Ψ^{rec} in comparison to the true phase screen density Ψ.

Mutual information $\mathrm{MI}(X, Y)$ measures the reduction in uncertainty of one random variable, Y, given knowledge of another variable, X [25]. The underlying concept for MI is entropy $H(Y)$ defined as follows:

$$H(Y) = -\sum_{y \in Y} p(y) \log p(y), \tag{29}$$

where $p(\cdot)$ represents the probability measure of Y. While $H(Y)$ quantifies the uncertainty of Y, $\mathrm{MI}(X, Y)$ describes the reduction of this uncertainty due to knowledge of X:

$$\mathrm{MI}(X, Y) = H(Y) - H(Y|X) = \sum_{x \in X, y \in Y} p(x, y) \log\left(\frac{p(x, y)}{p(x)p(y)}\right). \tag{30}$$

This metric vanishes, that is, $\mathrm{MI}(X, Y) = 0$, when X and Y are independent such that $p(x, y) = p(x)p(y)$, indicating no gain of information about Y due to the knowledge of X. For the opposite extreme, $\mathrm{MI}(X, Y)$ reaches $H(Y)$ when $X = Y$, indicating total predictability. In our study, a high value of $\mathrm{MI}(X_i, \mathrm{PD})/H(\mathrm{PD})$ for a given factor X_i signifies a greater reduction in uncertainty about PD, pointing to that factor's influence on PD.

For this study, we generated 5000 instances of the optimisation problem via Latin hypercube sampling, with all nine input factors (turbulence intensity, clutter, noise, and phase shifts of the six harmonics) varying simultaneously. MI was estimated using 250 nearest neighbours (or 5% of the total number of realisations) to approximate the probabilities $p(X_i)$ and $p(\mathrm{PD})$ and, consequently, their joint probability $p(X_i, \mathrm{PD})$. This choice of a relatively large subsample size is due to the high unexplained variance between the values of the input factors and PD: while introducing a higher bias, it reduced variance and provided stable MI estimates across larger bin sizes (e.g., MI results were consistent with those for 200 and 300 nearest neighbours).

The ranges of the stochastic parameters were chosen as follows: $||\Psi|| \in [\pi/5, 2\pi]$, $\sigma_C \in [0.009, 0.177]$, and $\sigma_N \in [0.009, 0.177]$. Figure 12 shows that the average clutter reflectivity (σ_C) and the phase shift of the longest harmonic (φ_1) have the largest influence on PD. In this experiment, $H(\mathrm{PD}) \approx 1.64$, whereas $\mathrm{MI}(\sigma_C, \mathrm{PD}) \approx 0.169$, $\mathrm{MI}(\varphi_1, \mathrm{PD}) \approx 0.01$, and $\mathrm{MI}(||\Psi||, \mathrm{PD}) \approx 0.005$. We have

$$\frac{\mathrm{MI}(\sigma_C, \mathrm{PD})}{H(\mathrm{PD})} \approx \frac{0.169}{1.64} \approx 0.1.$$

In other words, only about 10% of the uncertainty of PD is explained by σ_C and another 0.9% of the uncertainty is explained by the leading phase shift and $||\Psi||$. These findings suggest that among the parameters we analysed, there is no single one that can be used to predict the level of residual distortions. In other words, the resulting quality of focusing is determined by the combination of these and probably other parameters, such as the particular realisation of clutter reflectivity. This underlines the importance of statistical approach to the problem.

5.4 | Assessing Image Improvement due to Autofocus

The core assumption about the cost function defined in Equation (24) is that its minimisation leads to an image with sharp peaks that closely resembles the true image. To demonstrate the improvement of image quality with respect to the initial guess of zero amplitudes for Ψ^{rec}, we plot the differences in quality metrics between the uncorrected (i.e., initial) and autofocused images, denoted by $\Delta\mathrm{NCC}$, $\Delta\mathrm{ISLR}$, and $\Delta\mathrm{PD}$, against the corresponding changes in the cost function. In this study, we generate 1000 realisations of $\Psi(s)$ according to Equation (15) at fixed levels of $\nu_{\mathrm{clutter}}(z)$, see Equation (19). The noise vector, $\nu_{\mathrm{noise}}(x)$, is kept unchanged from the baseline realisation due to its insignificant impact on the success of autofocus, thus allowing us to focus on isolating the effects of $||\Psi||$ and σ_C.

Different rows in Figure 13 present this analysis for different clutter intensities by scaling ν_{clutter} to $\sigma_C = 0.0$, $\sigma_C = 0.09$, and $\sigma_C = 0.18$ for the top, middle, and bottom rows, respectively.

Different columns in Figure 13 demonstrate the focusing effect in terms of a change in the value of one image quality metric. We associate the improvement of image quality with $\Delta\mathrm{NCC} > 0$, $\Delta\mathrm{ISLR} < 0$, and $\Delta\mathrm{PD} < 0$, and draw a horizontal red line at the corresponding threshold. To further illustrate the impact of Ψ-

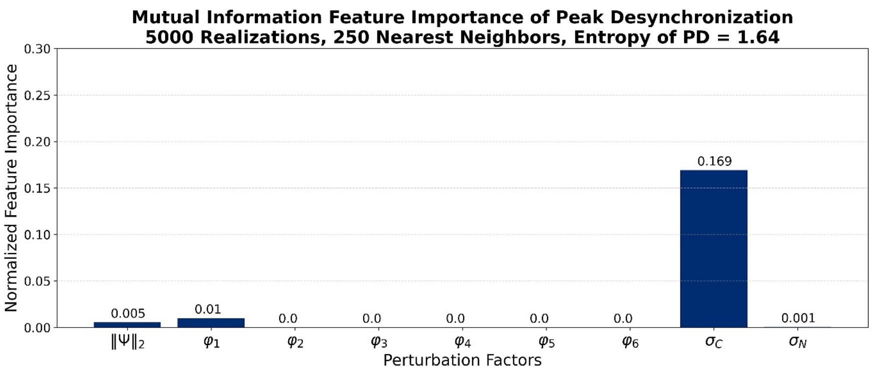

FIGURE 12 | Feature importance analysis based on the concept of mutual information, with the peak desynchronisation (PD) as the metric.

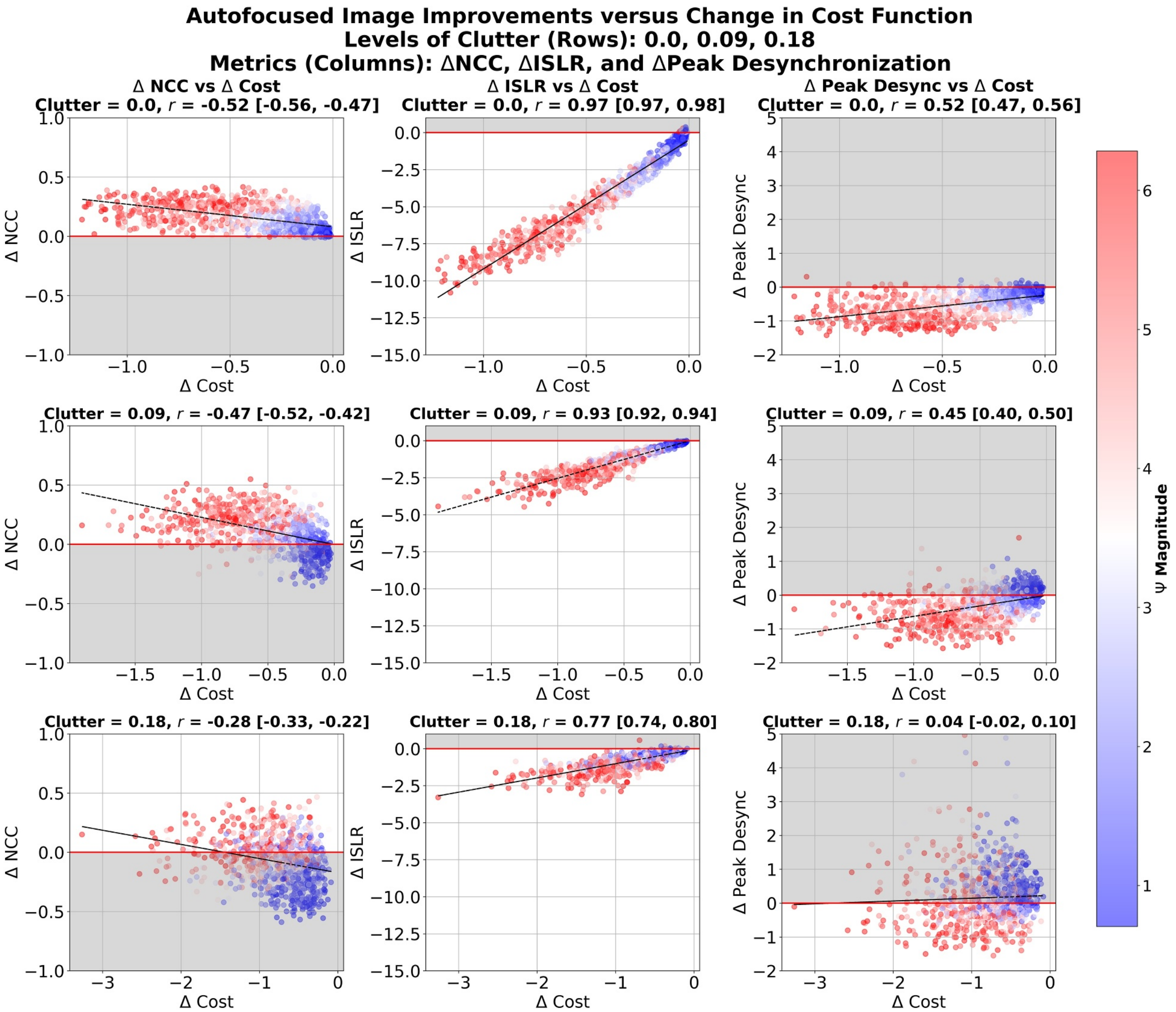

FIGURE 13 | Scatter plots depicting changes in each image quality metric versus the change of the cost value due to optimisation, with blue to red colours indicating increasing Ψ-magnitude in the range from $\pi/5$ to 2π.

TABLE 3 | The number of observed improvements out of 1000 realisations for each quality metric across different clutter levels.

Clutter (σ_C)	ΔNCC > 0	ΔISLR < 0	ΔPD < 0	All metrics improve	All metrics deteriorate
0	976	968	896	873	0
0.09	730	999	708	673	0
0.18	346	989	435	299	8

magnitude on the focusing outcome, each scatter point is colour-coded from blue to red according to the value of $||\Psi||$. Note that there are instances where certain quality metrics worsen, exemplified by Figure 10 where ISLR improves, but NCC and PD degrade. Table 3 presents a summary of the behaviour of individual metrics for different values of clutter, as well as the number of cases where all metrics improve simultaneously.

Returning to Figure 13, we make an observation that for small values of Ψ-magnitude (blue circles), the changes in all metrics, as well as in the cost value, are smaller that those for high Ψ-magnitude (red circles). This can be expected because the smaller the phase perturbation, the lower the potential gain from compensating it. At the same time, for high clutter we observe a significant number of cases with a moderate worsening of NCC and PD due to focusing. The latter may be explained by the low sensitivity of the cost function (24) to the geometric distortions, as it was already mentioned in Section 5.1.

On the contrary, high values of Ψ-magnitude result in a low-quality $\mathcal{I}^{\text{init}}$ due to the initial guess at $\Psi^{\text{rec}} = 0$, leaving a significant room for improvement in terms of the metric and cost values. A significant number of cases with $\Delta\text{NCC} < 0$ and $\Delta\text{PD} > 0$ for $\sigma_C = 0.18$ may indicate a higher probability of failure of the optimisation process where a local rather than global minimum of the cost function has been reached.

Among the three metrics analysed, ISLR is found to exhibit the highest correlation with the cost, as specified by the values of the correlation coefficient r. This is not surprizing because similarly to ISLR, the cost function is associated with the peak sharpness [23, 24]. Interestingly, a very high correlation ($r > 0.75$) is also observed for all values of clutter where two other metrics demonstrate a significant spread for a fixed value of ΔCost. At the same time, the ISLR gain for high-clutter setups is consistently lower than that for low clutter, unlike the gain in the cost. Note that usage of ISLR in the cost function is problematic due to its nonsmooth dependence on the control variables [9].

6 | Conclusions

We have developed a methodology for statistical assessment of the effectiveness of transionospheric SAR autofocus via numerical simulation. The optimisation-based autofocus algorithm developed in ref. [9] has been analysed and its effectiveness evaluated for a range of input parameters. Effectiveness, sensitivity, and weaknesses of various metrics of image quality have been explored.

In particular, we have observed that for long-wavelength spaceborne SAR, the optimisation-based autofocus demonstrates satisfactory performance in a significant majority of cases for all reasonable levels of phase perturbations due to the ionospheric turbulence. We have established that the focusing outcomes may have a significant spread in terms of the final values of image quality metrics, and the quality of the individual focused image cannot be reliably predicted using the value of a single parameter. Statistically, the most problematic are the scenes with high level of clutter where the gradient-based optimiser may fail to converge to the global minimum of the specified cost function.

Further directions of research may include the following.

- Convergence of the gradient-based optimiser to local minima that hampers autofocus performance warrants further analysis and adoption of robust global minimisation procedures based on methods such as multi-start, swarm, genetic algorithms, etc.
- Further refinement and customisation of the optimisation problem, including the use of additional cost functions (e.g., based on total variation), as well as convexification.
- Extended analysis of external factors affecting the performance, including the spatial spectrum of turbulence. In particular, the true Kolmogorov's spectrum can be used.
- Alternative ways of representing the perturbation and reconstruction screen density function, e.g., splines or wavelets.
- Incorporation of more sophisticated reflectivity models such as extended targets and textured background.
- Analysis of two-dimensional targets and phase screens, as well as modelling of a 'thick' ionosphere, e.g., by means of multiple phase screens.
- Studying the efficiency of the proposed autofocus procedure under generalised anisotropy of SPE in two-dimensional settings.
- Use of additional techniques that would emphasise the contribution from bright point scatterers and de-emphasise clutter and noise (e.g., compressive sensing).
- Utilising optimisation priors, for example, in the form of prior images with identifiable point or persistent scatterers [26] and maps of the imaged area.

Author Contributions

Patrick Haughey: data curation, formal analysis, investigation, methodology, software, visualization, writing – original draft. **Mikhail Gilman:** conceptualization, supervision, validation, writing – review and editing. **Semyon Tsynkov:** conceptualization, funding acquisition, project administration, resources, supervision, validation, writing – review and editing.

Conflicts of Interest

The authors declare no conflicts of interest.

Data Availability Statement

The authors have nothing to report.

Endnotes

[1] Due to the Rayleigh modelling of the complex clutter vectors in this study, the clutter range considered is scaled to $\frac{\sqrt{\pi}}{2}[0.01, 0.2]$ to remain consistent with the clutter modelling in [9].

References

1. I. Walterscheid, P. Berens, M. Caris, et al., "First Results of a Joint Measurement Campaign With PAMIR-Ka and MIRANDA-94," in *2020 IEEE Radar Conference (RadarConf20)* (IEEE, 2020), 1–6.

2. N. A. Armand and V. Mikhailovich Polyakov, *Radio Propagation and Remote Sensing of the Environment* (CRC Press, 2004).

3. E. M. Smith and S. V. Tsynkov, "Dual Carrier Probing for Spaceborne SAR Imaging," *SIAM Journal on Imaging Sciences* 4, no. 2 (2011): 501–542, https://doi.org/10.1137/10078325x.

4. M. Gilman, E. Smith, and S. Tsynkov, "Reduction of Ionospheric Distortions for Spaceborne Synthetic Aperture Radar With the Help of Image Registration," *Inverse Problems* 29, no. 5 (May 2013): 054005, https://doi.org/10.1088/0266-5611/29/5/054005.

5. M. Gilman, E. Smith, and S. Tsynkov, *Transionospheric Synthetic Aperture Imaging* (Birkhäuser/Springer, 2017): Applied and Numerical Harmonic Analysis.

6. D. E. Wahl, P. H. Eichel, D. C. Ghiglia, and C. V. Jakowatz, Jr, "Phase Gradient Autofocus — A Robust Tool for High Resolution SAR Phase Correction," *IEEE Transactions on Aerospace and Electronic Systems* 30, no. 3 (1994): 827–835, https://doi.org/10.1109/7.303752.

7. C. V. Jakowatz, Jr., D. E. Wahl, P. H. Eichel, D. C. Ghiglia, and P. A. Thompson, *Spotlight-Mode Synthetic Aperture Radar: A Signal Processing Approach* (Springer, 1996).

8. I. G. Cumming and F. H. Wong, *Digital Processing of Synthetic Aperture Radar Data* (Artech House, 2005): Algorithms and Implementation.

9. M. Gilman and S. V. Tsynkov, "Transionospheric Autofocus for Synthetic Aperture Radar," *SIAM Journal on Imaging Sciences* 16, no. 4 (2023): 2144–2174, https://doi.org/10.1137/22m153570x.

10. J. Su Kim, K. P. Papathanassiou, R. Scheiber, and S. Quegan, "Correcting Distortion of Polarimetric SAR Data Induced by Ionospheric Scintillation," *IEEE Transactions on Geoscience and Remote Sensing* 53, no. 12 (2015): 6319–6335, https://doi.org/10.1109/tgrs.2015.2431856.

11. Y. Ji, Z. Dong, Y. Zhang, C. Wang, C. Hu, and Z. Xu, "Transionospheric Synthetic Aperture Radar Observation: A Comprehensive Review," *IEEE Geoscience and Remote Sensing Magazine* (2024): 2–43, https://doi.org/10.1109/mgrs.2024.3454635.

12. M. Cheney, "A Mathematical Tutorial on Synthetic Aperture Radar," *SIAM Review* 43, no. 2 (2001): 301–312: (electronic), https://doi.org/10.1137/s0036144500368859.

13. M. Gilman and S. Tsynkov, "Modeling the Earth's Ionosphere by a Phase Screen for the Analysis of Transionospheric SAR Imaging," *IEEE Transactions on Geoscience and Remote Sensing* 62 (2024): 1–16: Article Sequence Number 2000216 (16 pp), https://doi.org/10.1109/tgrs.2023.3335146.

14. M. Gilman and S. Tsynkov, "Vertical Autofocus for the Phase Screen in a Turbulent Ionosphere," *Inverse Problems* 39, no. 36pp (2023): 045001, https://doi.org/10.1088/1361-6420/acb8d6.

15. M. Gilman and S. Tsynkov, "Mathematical Analysis of SAR Imaging Through a Turbulent Ionosphere," in *Application of Mathematics in Technical and Natural Sciences: 9th International Conference for Promoting the Application of Mathematics in Technical and Natural Sciences — AMiTaNS'17, Volume 1895 of AIP Conference Proceedings*, ed. M. D. Todorov (American Institute of Physics (AIP), 2017): page 020003 (23pp).

16. C. L. Rino, "A Power Law Phase Screen Model for Ionospheric Scintillation: 1. Weak Scatter," *Radio Science* 14, no. 6 (1979): 1135–1145, https://doi.org/10.1029/rs014i006p01135.

17. Y. Ji, Z. Dong, Y. Zhang, and Q. Zhang, "An Autofocus Approach With Applications to Ionospheric Scintillation Compensation for Spaceborne SAR Images," *IEEE Transactions on Aerospace and Electronic Systems* 58, no. 2 (2021): 989–1004, https://doi.org/10.1109/taes.2021.3108117.

18. M. Gilman and S. Tsynkov, "Comparative Analysis of Performance for Optimization-Based Transionospheric SAR Autofocus," *Radio Science* 60, no. 2 (2025): 2024RS008168, https://doi.org/10.1029/2024rs008168.

19. Y. Ji, C. Yu, Q. Zhang, Z. Dong, Y. Zhang, and Y. Wang, "An Ionospheric Phase Screen Projection Method of Phase Gradient Autofocus in Spaceborne SAR," *IEEE Geoscience and Remote Sensing Letters* 19 (2022): 1–5, https://doi.org/10.1109/lgrs.2022.3147036.

20. V. L. Ginzburg, *The Propagation of Electromagnetic Waves in Plasmas, Volume 7 of International Series of Monographs on Electromagnetic Waves* (Pergamon Press, 1964).

21. S. M. Rytov, Yu. A. Kravtsov, and V. I. Tatarskii, *Principles of Statistical Radiophysics. Volume 3. Elements of Random Fields* (Springer-Verlag, 1989): Translated from the second Russian edition by Alexander P. Repyev.

22. A. S. Monin and A. M. Yaglom, *Statistical Fluid Mechanics: Mechanics of Turbulence*, Vol. 1 (MIT Press, 1971).

23. R. L. Morrison, M. N. Do, and D. C. Munson, "SAR Image Autofocus by Sharpness Optimization: A Theoretical Study," *IEEE Transactions on Image Processing* 16, no. 9 (2007): 2309–2321, https://doi.org/10.1109/tip.2007.903252.

24. R. A. Muller and A. Buffington, "Real-Time Correction of Atmospherically Degraded Telescope Images Through Image Sharpening," *JOSA* 64, no. 9 (1974): 1200–1210, https://doi.org/10.1364/josa.64.001200.

25. A. Kraskov, H. Stögbauer, and P. Grassberger, "Estimating Mutual Information," *Physical Review E: Statistical, Nonlinear, and Soft Matter Physics* 69, no. 6 (2004): 066138.

26. M. Crosetto, O. Monserrat, M. Cuevas-González, N. Devanthéry, and B. Crippa, "Persistent Scatterer Interferometry: A Review," *ISPRS Journal of Photogrammetry and Remote Sensing* 115 (2016): 78–89, https://doi.org/10.1016/j.isprsjprs.2015.10.011.

Appendix A: Gradient of the Cost Function

We start by rewriting Formula (24) for the cost function:

$$\begin{aligned}\mathrm{Cost}(\mathbf{p}^{\mathrm{rec}},\mathbf{q}^{\mathrm{rec}}) = -\delta_x\sum_{i=1}^{M}|\mathcal{I}(y_i;\Psi^{\mathrm{rec}}(\cdot\,;\mathbf{p}^{\mathrm{rec}},\mathbf{q}^{\mathrm{rec}}))|^4 \\ +\zeta\sum_{n=1}^{N^{\mathrm{rec}}}k_n^2\Big(\big(p_n^{\mathrm{rec}}\big)^2+\big(q_n^{\mathrm{rec}}\big)^2\Big)\Big),\end{aligned} \tag{A1}$$

where $M = |\{y_i\}|$ is the cardinality of the spatial domain of the image. The control variables are the components of the vectors $\mathbf{p}^{\mathrm{rec}}$ and $\mathbf{q}^{\mathrm{rec}}$, that is, the Fourier amplitudes p_n^{rec} and q_n^{rec} for $n = 1, \ldots, N^{\mathrm{rec}}$.

Using the shortcut notation $I_i = \mathcal{I}(y_i;\Psi^{\mathrm{rec}}(\cdot\,;\mathbf{p}^{\mathrm{rec}},\mathbf{q}^{\mathrm{rec}}))$, we present the expressions for the partial derivatives of the cost function (A1) with respect to the Fourier amplitudes corresponding to the n^{th} harmonic:

$$\begin{aligned}\frac{\partial}{\partial p_n^{\mathrm{rec}}}\mathrm{Cost}(\mathbf{p}^{\mathrm{rec}},\mathbf{q}^{\mathrm{rec}}) &= -\delta_x\sum_{i=1}^{M}\frac{\partial}{\partial p_n^{\mathrm{rec}}}\big(|I_i|^2\big)^2 + 2\zeta k_n^2 p_n^{\mathrm{rec}},\\ \frac{\partial}{\partial q_n^{\mathrm{rec}}}\mathrm{Cost}(\mathbf{p}^{\mathrm{rec}},\mathbf{q}^{\mathrm{rec}}) &= -\delta_x\sum_{i=1}^{M}\frac{\partial}{\partial q_n^{\mathrm{rec}}}\big(|I_i|^2\big)^2 + 2\zeta k_n^2 q_n^{\mathrm{rec}}.\end{aligned} \tag{A2}$$

The partial derivatives in Equation (A2) can be expressed as follows:

$$\begin{aligned}\frac{\partial}{\partial p_n^{\mathrm{rec}}}\big(|I_i|^2\big)^2 = 2|I_i|^2\left(\bar{I}_i\frac{\partial I_i}{\partial p_n^{\mathrm{rec}}}+I_i\frac{\partial \bar{I}_i}{\partial p_n^{\mathrm{rec}}}\right),\quad \frac{\partial}{\partial q_n^{\mathrm{rec}}}\big(|I_i|^2\big)^2\\ = 2|I_i|^2\left(\bar{I}_i\frac{\partial I_i}{\partial q_n^{\mathrm{rec}}}+I_i\frac{\partial \bar{I}_i}{\partial q_n^{\mathrm{rec}}}\right),\end{aligned} \tag{A3}$$

where the overbar denotes complex conjugate.

In turn, the partial derivatives of I_i in Equation (A3) can be found from Formula (14) recast as

$$\begin{aligned}I_i &= \frac{1}{F}\int u(x)\exp\left[-\frac{\mathrm{i}\pi}{F}(x-y_i)^2+\mathrm{i}\Psi^{\mathrm{rec}}(s(x,y_i);\mathbf{p}^{\mathrm{rec}},\mathbf{q}^{\mathrm{rec}})\right]w_{\mathcal{I}}(x-y_i)\,\mathrm{d}x\\ &\equiv \int\mathcal{K}_i(x)\exp[\mathrm{i}\Psi^{\mathrm{rec}}(s(x,y_i);\mathbf{p}^{\mathrm{rec}},\mathbf{q}^{\mathrm{rec}})]\,\mathrm{d}x,\\ \bar{I}_i &= \frac{1}{F}\int u(x)\,\exp\left[\frac{\mathrm{i}\pi}{F}(x-y_i)^2-\mathrm{i}\Psi^{\mathrm{rec}}(s(x,y_i);\mathbf{p}^{\mathrm{rec}},\mathbf{q}^{\mathrm{rec}})\right]w_{\mathcal{I}}(x-y_i)\,\mathrm{d}x\\ &\equiv \int\overline{\mathcal{K}_i(x)}\exp[-\mathrm{i}\Psi^{\mathrm{rec}}(s(x,y_i);\mathbf{p}^{\mathrm{rec}},\mathbf{q}^{\mathrm{rec}})]\,\mathrm{d}x,\end{aligned}$$

where

$$\mathcal{K}_i(x) = \frac{1}{F}u(x)\exp\left[-\frac{\mathrm{i}\pi}{F}(x-y_i)^2\right]w_{\mathcal{I}}(x-y_i).$$

Accordingly,

$$\begin{aligned}\frac{\partial I_i}{\partial p_n^{\mathrm{rec}}} &= \mathrm{i}\int\mathcal{K}_i(x)\exp[\mathrm{i}\Psi^{\mathrm{rec}}(s(x,y_i);\mathbf{p}^{\mathrm{rec}},\mathbf{q}^{\mathrm{rec}})]\frac{\partial\Psi^{\mathrm{rec}}(s(x,y_i);\mathbf{p}^{\mathrm{rec}},\mathbf{q}^{\mathrm{rec}})}{\partial p_n^{\mathrm{rec}}}\,\mathrm{d}x,\\ \frac{\partial \bar{I}_i}{\partial p_n^{\mathrm{rec}}} &= -\mathrm{i}\int\overline{\mathcal{K}_i(x)}\exp[-\mathrm{i}\Psi^{\mathrm{rec}}(s(x,y_i);\mathbf{p}^{\mathrm{rec}},\mathbf{q}^{\mathrm{rec}})]\frac{\partial\Psi^{\mathrm{rec}}(s(x,y_i);\mathbf{p}^{\mathrm{rec}},\mathbf{q}^{\mathrm{rec}})}{\partial p_n^{\mathrm{rec}}}\,\mathrm{d}x.\end{aligned} \tag{A4}$$

Two other partial derivatives in Equation (A3) are obtained by replacing $\partial/\partial p_n^{\text{rec}}$ with $\partial/\partial q_n^{\text{rec}}$ in Equation (A4).

Further, the counterpart to Formula (15) for Ψ^{rec} has the following form:

$$\Psi^{\text{rec}}(s(x,y_i);\mathbf{p}^{\text{rec}},\mathbf{q}^{\text{rec}}) = \sum_{n=1}^{N^{\text{rec}}}\left[p_n^{\text{rec}}\cos(k_n s(x,y_i)) + q_n^{\text{rec}}\cos(k_n s(x,y_i))\right],$$

and hence,

$$\begin{aligned} \frac{\partial\Psi^{\text{rec}}(s(x,y_i);\mathbf{p}^{\text{rec}},\mathbf{q}^{\text{rec}})}{\partial p_n^{\text{rec}}} &= \cos(k_n s(x,y_i)). \\ \frac{\partial\Psi^{\text{rec}}(s(x,y_i);\mathbf{p}^{\text{rec}},\mathbf{q}^{\text{rec}})}{\partial q_n^{\text{rec}}} &= \sin(k_n s(x,y_i)). \end{aligned} \tag{A5}$$

Substituting Equations (A3)–(A5) into Equation (A2), we obtain expressions for the components of the cost function gradient required by the optimiser.

Appendix B: Shift of the Image Due to Linear Phase

We demonstrate that the perturbation $\Psi(s(x,z))$ that is linear in the screen coordinate results in an azimuthal shift of the image that is proportional to the slope of Ψ. Consider a single point scatterer $\nu(z) = \delta(z)$, where $\delta(z)$ is the Dirac delta function. We define $\Psi(s(x,z)) = ms$, with $m \in \mathbb{R}$, where $s(x,z) = \xi x + (1-\xi)z$ for some relative screen elevation $\xi \in [0,1]$. Substituting the signal definition from Equation (11) into the expression for SAR image in Equation (14) and using the rectangular window w^{rect}, see Equation (13), we obtain

$$\begin{aligned} \mathcal{I}(y) = &\iint w^{\text{rect}}(x-y)w^{\text{rect}}(x-z)\exp\left(\mathrm{i}\frac{\pi}{F}\left[(x-z)^2-(x-y)^2\right]\right) \\ &\exp(-\mathrm{i}m[\xi x + (1-\xi)z])\delta(z)\,\mathrm{d}z\,\mathrm{d}x \\ = &\int w^{\text{rect}}(x-y)w^{\text{rect}}(x)\exp\left(\mathrm{i}\frac{\pi}{F}\left[x^2-(x-y)^2\right]\right)\exp(-\mathrm{i}m\xi x)\,\mathrm{d}x \end{aligned} \tag{A6}$$

Similarly to Equations (11) and (14), the product of the characteristic functions in Equation (A6) restricts the integration domain. For a given $y \in \mathbb{R}$, the integration bounds are $x \in [L(y), U(y)]$, where:

$$L(y) = \max\left(-\frac{F}{2},\ y-\frac{F}{2}\right), \quad U(y) = \min\left(\frac{F}{2},\ y+\frac{F}{2}\right). \tag{A7}$$

To ensure $L(y) \le U(y)$, we restrict the image domain to $|y| \le F$. Outside of it, we get $\mathcal{I}(y) \equiv 0$ because the supports of the window functions in Equation (A6) do not intersect.

The exponential in Equation (A6) can be factored as:

$$\exp\left(\mathrm{i}\frac{\pi}{F}(2xy-y^2) - im\xi x\right) = \exp\left(-\mathrm{i}\frac{\pi}{F}y^2\right)\exp\left[\mathrm{i}\frac{2\pi x}{F}\left(y-\frac{Fm\xi}{2\pi}\right)\right] \tag{A8}$$

Defining

$$\tilde{y} = y - \frac{Fm\xi}{2\pi}, \tag{A9}$$

We transform Equation (A6) into

$$\mathcal{I}(y) = \exp\left(-\mathrm{i}\frac{\pi}{F}y^2\right)\int_{L(y)}^{U(y)}\exp\left(\mathrm{i}\frac{2\pi x\tilde{y}}{F}\right)\mathrm{d}x. \tag{A10}$$

In order to simplify Equation (A10), we centre the integration interval by introducing the midpoint $M(y) = \frac{1}{2}(L(y)+U(y)) = \frac{y}{2}$ and width $\tilde{F}(y) = U(y) - L(y) = F - |y|$. Introducing $\tilde{x}$ such that $x = M(y) + \tilde{x}$ and $\tilde{x} \in \left[-\tilde{F}(y)/2, \tilde{F}(y)/2\right]$, we obtain:

$$\begin{aligned} \mathcal{I}(y) &= \exp\left(-\mathrm{i}\frac{\pi}{F}y^2\right)\exp\left(\mathrm{i}\frac{2\pi M(y)\tilde{y}}{F}\right)\int_{-\tilde{F}(y)/2}^{\tilde{F}(y)/2}\exp\left(\mathrm{i}\frac{2\pi x\tilde{y}}{F}\right)\mathrm{d}\tilde{x} \\ &= \exp\left(-\mathrm{i}\frac{\pi}{F}y^2\right)\exp(-\mathrm{i}2\pi M(y)\tilde{y})\tilde{F}(y)\,sinc\left(\pi\frac{\tilde{F}(y)}{F}\tilde{y}\right), \end{aligned} \tag{A11}$$

where $sinc(x) = \sin(x)/x$. From Equations (A9) and (A11), it can be seen that the central peak of $|\mathcal{I}(y)|$ corresponds to $\tilde{y} = 0$, that is, $y = \frac{Fm\xi}{2\pi}$. Given that the point scatterer $\nu(z) = \delta(z)$ is located at $z = 0$, this formula yields the expression for the shift magnitude due to a linear phase screen density function $\Psi(s) = ms$.